
Programmable 3D snapshot microscopy with Fourier convolutional networks

Diptodip Deb¹Zhenfei Jiao¹Alex B. Chen^{1,2}Misha B. Ahrens^{1,†}Kaspar Podgorski^{1,†}Srinivas C. Turaga^{1,†}¹ HHMI Janelia Research Campus, ² Harvard University

{debd, ahrensm, podgorskik, turagas}@janelia.hhmi.org

zfjiao@hust.edu.cn

abchen@g.harvard.edu

† equal contribution

Abstract

3D snapshot microscopy enables fast volumetric imaging by capturing a 3D volume in a single 2D camera image, and has found a variety of biological applications such as whole brain imaging of fast neural activity in larval zebrafish. The optimal microscope design for this optical 3D-to-2D encoding is both sample- and task-dependent, with no general solution known. Highly programmable optical elements create new possibilities for sample-specific computational optimization of microscope parameters, e.g. tuning the collection of light for a given sample structure. We perform such optimization with deep learning, using a differentiable wave-optics simulation of light propagation through a programmable microscope and a neural network to reconstruct volumes from the microscope image. We introduce a class of global kernel Fourier convolutional neural networks which can efficiently decode information from multiple depths in the volume, globally encoded across a 3D snapshot image. We show that our proposed networks succeed in large field of view volume reconstruction and microscope parameter optimization where traditional networks fail. We also show that our networks outperform the state-of-the-art learned reconstruction algorithms for lensless computational photography.

1 Introduction

Volumetric imaging has been a valuable technique for measuring neural activity at single neuron resolution across the brain [1–3]. Existing approaches to whole-brain imaging involve sequential acquisition of stacks of 2D images [1], typically resulting in 0.5Hz - 2Hz volume capture rates, limited by the number of 2D depth plane acquisitions. However, since neural activity occurs at orders of magnitude faster timescales, faster volume imaging rates can provide understanding of neural computations with significantly more detail.

3D snapshot microscopy can speed up the imaging of a 3D sample volume by optically encoding images corresponding to different depth planes in the volume into a single 2D image, allowing for fast volume acquisition at the frame rate of the camera sensor followed by computational decoding to reconstruct the 3D volume [4–17]. However, the optimal optical design for a 3D snapshot microscope implementing the 3D-to-2D encoding is unknown in general [4], and likely depends on the specific sample structure. In a parallel to early computer vision, existing 3D snapshot microscopes have been hand designed with fixed optical elements and not optimized for particular imaging

conditions. Newly developed programmable microscopes enable the implementation of a rich space of microscope transfer functions, and present the possibility of direct optimization of snapshot microscope parameters specifically for particular classes of samples and imaging tasks. Analogous to the modern machine learning era of optimizing richly parameterized deep learning architectures for specific tasks, we hope that optimizing richly parameterized programmable microscopes will enable a new era of high performance microscopy.

Programmable optical elements such as spatial light modulators (SLM) and deformable mirrors can have up to 10^6 free parameters and represent complex transformations of the light field propagating inside a microscope. In this work, we consider the case of a high pixel count SLM implementing a phase mask placed in the pupil (Fourier plane) of the microscope. In principle, a programmable microscope constructed in this manner can be made to approximate more standard microscopes comprised of fixed optical elements including standard mirrors and lenses.

Problem statement We wish to computationally optimize the parameters of a programmable microscope (**optical encoder**) and a reconstruction network (**computational decoder**). By formulating the problem as the end-to-end optimization of such a physics-based **autoencoder**, we can jointly optimize both the microscope and the reconstruction network. Given a 3D volume \mathbf{v} , we want to capture a single 2D camera image \mathbf{c} (**bottleneck**) from a simulated microscope \mathbf{M}_ϕ , parameterized by ϕ . From this image \mathbf{c} , we want to reconstruct an estimate of the 3D volume $\hat{\mathbf{v}}$ using a reconstruction neural network \mathbf{R}_θ parameterized by θ (Figure 1A). This is an autoencoder where the encoder happens to be a wave-optics simulation of the microscope, the parameters of which can be jointly optimized along with the decoder network. Both the parameters of the microscope as well as the computational reconstruction algorithm will affect the quality of the reconstruction $\hat{\mathbf{v}}$.

1.1 Prior work

3D snapshot microscopy A pioneering strategy in 3D snapshot microscopy has been light field microscopy [9], which employs an array of microlenses inserted near the microscope’s image plane to create subimages on the camera sensor, which enable the measurement of both the amplitude and direction of light rays that would have arrived at a camera pixel [9, 18]. A variety of microlens-array-based light field microscopes have been used to perform whole-brain imaging [3, 7, 9, 13–15, 17, 19]. While the details of these designs vary, microlens-based designs have, to various degrees, three main limitations that can be improved: 1) blocking or scattering of light between microlenses, causing light inefficiency, 2) not making use of all pixels on the camera to encode a 3D sample, leading to inefficient compression and suboptimal reconstructions $\hat{\mathbf{v}}$ and 3) a fixed optical encoding scheme that cannot be tuned to the known structure of the sample.

An alternative to using microlenses is to implement a phase mask or diffuser to spread light broadly across the camera sensor [4–6, 8, 10, 11, 16]. These phase masks can be optimized for specific imaging problems and can be programmable, allowing different microscope parameters to be used for different samples. Optimization of these masks has a long history in holography [20–22], but in the context of snapshot microscopy has largely been performed either for very sparse samples or in restricted parameter spaces for simple surrogate objectives [16].

Reconstruction algorithms for 3D snapshot microscopy All of the discussed snapshot microscope designs require computational reconstruction to produce an estimate of the sample volume. Conventionally, volume reconstruction has been performed via an iterative optimization algorithm, e.g. based on Richardson-Lucy (R-L) deconvolution [23–25]. This requires a simulation of the imaging process and an initial estimate of the sample volume, then repeatedly updates the estimated volume based on the error between observed and expected 2D images until the estimated volume has converged.

Not only is this iteration slow to produce reconstructions, especially in the case that many volumes need to be reconstructed (e.g. for whole-brain activity imaging), it is practically difficult to propagate gradients through the many iterations required to produce a good reconstruction due to the memory required and vanishing gradients. For a training procedure in which microscope parameters are optimized over multiple reconstructions, an iterative reconstruction algorithm is therefore intractable to optimize via backpropagation of gradients. Recently, deep learning has been applied to reconstruction, sometimes by combining with or unrolling iterations of traditional deconvolution algorithms, providing the benefits of fast amortized inference and higher quality reconstructions due to learning of structural priors [12, 26–28].

Deep learning optimization of microscope parameters The use of deep learning for reconstruction has allowed successful optimization of diffuser or phase mask parameters in microscopy [16, 29]. However, these formulations either deal with sparse particle localization rather than volume reconstruction, sparse volumes, or optimize far fewer parameters than can be programmed using modern SLMs. This is due to the difficulty in reconstructing dense samples and in memory constraints of optimizing detailed simulations of microscopes with many parameters.

1.2 Our contributions

Therefore, we ask: can we computationally search a rich space of microscope parameters to find one optimal for a particular class of sample volumes? To explore this question, we used a 4f model of a microscope with a programmable phase mask (ϕ) implemented using a spatial light modulator (SLM) [29], described further in Appendix A.1. These phase masks ϕ can have over 10^6 parameters. We implemented a differentiable wave optics simulation in order to enable gradient-based optimization of ϕ . By framing the problem as a physics-based autoencoder, we jointly optimize both the microscope encoder and the neural network decoder. Our contributions are as follows:

1. Because light from a given 3D voxel can be encoded non-locally across the 2D camera image, we introduce an efficient new reconstruction network architecture using very large global convolutions implemented efficiently using Fourier convolutions.
2. We show that our networks outperform the state-of-the-art deep networks for both volume reconstruction and microscope parameter optimization, and for lensless computational photography reconstruction [12].
3. Our method enables, for the first time, direct end-to-end optimization of microscope parameters in the space of SLM pixels with over 10^6 parameters for 3D snapshot imaging.

2 Methods

Here we describe our proposed new network architectures, followed by a description of our autoencoder training of both the microscope parameters and reconstruction network (Figure 1A). The programmable microscope is simulated by a differentiable implementation of a wave-optics model of light propagation. We have selected a programmable microscope design based on pupil-plane phase modulation with a programmable spatial light modulator, for which imaging is well-approximated by a computationally-efficient convolution [30]. A detailed description of our simulation is provided in Appendix A.1.

2.1 FourierNet and FourierUNet architectures for volume reconstruction from camera images

Because the images created by snapshot microscopes can potentially encode signals from any plane in the volume to any location in the camera image, it is essential that a reconstruction network for decoding the camera image have global context. Existing multi-scale convolutional neural networks such as the UNet [31] do achieve global context, but at the expense of requiring many layers of computation with small convolution kernels and, as we show, have a local information bias which is inappropriate for computational optics.

FourierNet We propose a simple three layer convolutional network architecture with very large global convolutions at the very first layer, followed by two standard local convolutional layers (Figure 1B). We define a global convolution as a convolution with kernel size equal to the input image. Such a convolution achieves global context in a single step but is computationally expensive. We implement such global convolutions more efficiently in the Fourier domain, yielding a speed up of two orders of magnitude. Due to the use of Fourier convolutions to enable global context, we call our architecture FourierNet. The standard convolutions following the Fourier convolution are either 2D or 3D as needed. In contrast to a typical UNet which can contain many tens of convolution layers, the FourierNet is only three layers deep.

FourierUNet We also propose a multi-scale variant of the FourierNet by bringing together elements of the multi-scale UNet and the single-scale FourierNet. Here, we take advantage of the fact that down-sampling in image space corresponds to a simple cropping operation in the Fourier domain. Thus we

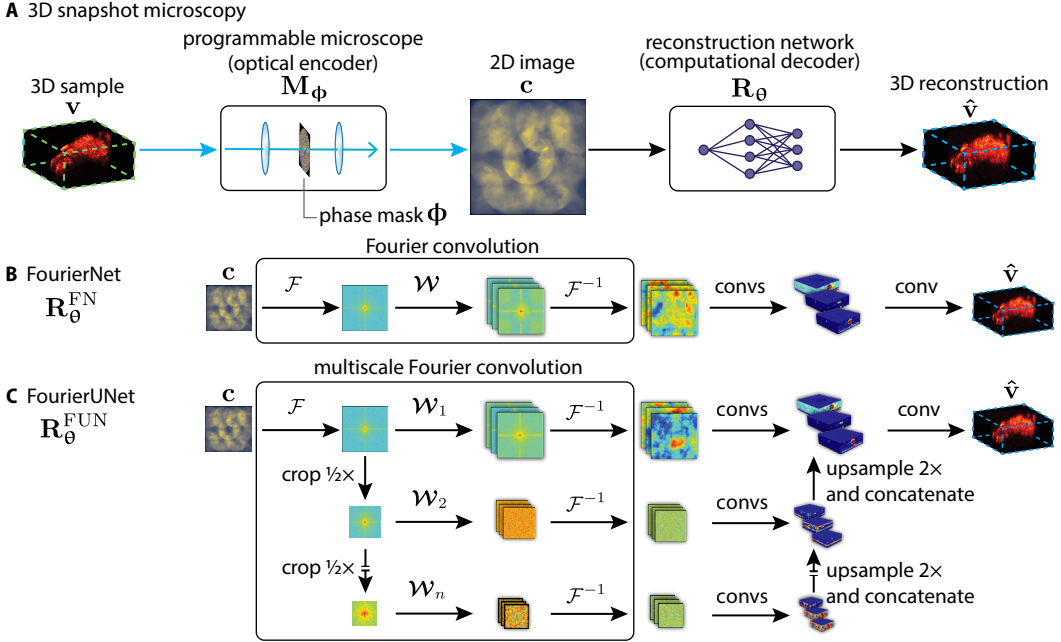


Figure 1: Overview of our problem setup and our proposed network architectures. Top row (A) shows the problem of 3D snapshot microscopy, where a 3D reconstruction of a 3D sample is computationally created from a 2D image. Middle row (B) shows our proposed FourierNet architecture, which includes a new **Fourier convolution** layer that enables efficient computation of global features. Bottom row (C) shows an extension of our proposed architecture, the FourierUNet, which mimics the multiscale feature extraction of a standard UNet efficiently and with global features using a **multiscale Fourier convolution**.

implement multi-scale global Fourier convolutions efficiently in the Fourier domain (Figure 1C) to replace the encoding/“analysis” pathway of a UNet. We then use the standard decoding/“synthesis” pathway of the UNet to combine the multi-scale features into a single 3D volume reconstruction. The “synthesis” pathway can either include 2D or 3D convolution layers as needed (Appendix A.3, A.4).

Fourier domain convolutions It is well-known that convolutions with large kernels can be implemented more efficiently in the Fourier domain [32–34]. A naive implementation of a global convolution kernel (a kernel of the same size as the input) requires $\mathcal{O}(N^2)$ operations, where N is number of pixels in both the image and the kernel. The well-known alternative to efficiently implement large convolution kernels is to Fourier transform the input \mathbf{x} and convolution kernel \mathbf{w} , perform an element-wise multiplication in Fourier space, followed by an inverse Fourier transform, requiring only $\mathcal{O}(N \log N)$ operations [33, 34]. We go further and directly store and optimize the weights in Fourier space \mathbf{W} to save one extra Fourier transform at the expense of $8 \times$ extra parameters (Appendix A.3).

$$\mathbf{w} * \mathbf{x} = \mathcal{F}^{-1} \{ \mathcal{F} \{ \mathbf{w} \} \odot \mathcal{F} \{ \mathbf{x} \} \} = \mathcal{F}^{-1} \{ \mathbf{W} \odot \mathcal{F} \{ \mathbf{x} \} \} \quad (1)$$

We find for image and kernel sizes of 256×256 , our implementation leads to nearly $500 \times$ speedup. The standard PyTorch convolution takes 2860ms, while our Fourier convolution takes 5.92ms on a TITAN X.

Multi-scale Fourier domain convolutions It is well-known [32] that an image can be downsampled by cropping the Fourier transform of the image. Thus the standard Fourier convolution can be extended to efficiently produce a multi-scale feature representation in the same step (Figure 1C). We define our multi-scale Fourier convolution as

$$\{ \mathcal{F}^{-1} \{ \mathbf{W}_1 \odot \text{crop}_1 [\mathbf{c}] \}, \mathcal{F}^{-1} \{ \mathbf{W}_2 \odot \text{crop}_2 [\mathbf{c}] \}, \dots, \mathcal{F}^{-1} \{ \mathbf{W}_n \odot \text{crop}_n [\mathbf{c}] \} \} \quad (2)$$

where the subscript denotes the scale of the multiscale Fourier convolution (higher subscript indicates lower spatial scale/more cropping in Fourier space) and we precompute $\mathbf{c} := \mathcal{F} \{ \mathbf{c} \}$ once.

2.2 Physics-based autoencoder for simultaneous optimization of microscope and reconstruction network

We describe the imaging process as the following transformation from the 3D light intensity volume of the sample \mathbf{v} to the 2D image formed on the camera \mathbf{c} :

$$\mu_c = M_\phi(\mathbf{v}) \quad (3)$$

$$\epsilon \sim \mathcal{N}(0, 1) \quad (4)$$

$$\mathbf{c} = \max([\mu_c + \sqrt{\mu_c}\epsilon], 0) \quad (5)$$

where M_ϕ denotes the microscope parameterized by a 2D phase mask, ϕ . This phase mask ϕ describes the 3D-to-2D encoding of this microscope model completely. A Poisson distribution with mean rate μ_c describes the physics of photon detection at the camera, but this noise distribution is not differentiable. We approximate this camera noise distribution with a rectified Gaussian. We include details on M_ϕ in Appendix A.1 [30].

Jointly training reconstruction networks and microscope parameters involves simulating the imaging, performing the reconstruction, then backpropagating gradients to update the reconstruction network and microscope parameters. Further details on how we parallelize such a model and support planewise reconstruction networks and planewise sparse gradient computation are provided in Appendix A.2.

Our loss function computes the normalized mean squared error (MSE) L_{HNMSE} between the high pass filtered sample and reconstruction weighted by the normalized MSE L_{NMSE} between the original sample and reconstruction (in order to ensure the network doesn't totally ignore the low frequency content of the reconstruction). Formally, our loss function $L(\mathbf{v}, \hat{\mathbf{v}})$ is defined:

$$L(\mathbf{v}, \hat{\mathbf{v}}) = L_{\text{HNMSE}}(\mathbf{v}, \hat{\mathbf{v}}) + \beta L_{\text{NMSE}}(\mathbf{v}, \hat{\mathbf{v}}) \quad (6)$$

$$L_{\text{HNMSE}}(\mathbf{v}, \hat{\mathbf{v}}) = \frac{\mathbb{E}[(H(\mathbf{v}) - H(\hat{\mathbf{v}}))^2]}{\mathbb{E}(H(\mathbf{v})^2)} \quad (7)$$

$$L_{\text{NMSE}}(\mathbf{v}, \hat{\mathbf{v}}) = \frac{\mathbb{E}[(\mathbf{v} - \hat{\mathbf{v}})^2]}{\mathbb{E}(\mathbf{v}^2)} \quad (8)$$

where $H(\cdot)$ denotes high pass filtering and $\mathbb{E}(\cdot)$ denotes computing the mean. Both loss terms are normalized as shown in order to reduce the variance of the loss, which can otherwise take on values of large magnitudes and cause instability during training. For our experiments, we set the weight β for the L_{NMSE} term to be 0.1.

In general, we first optimize microscope parameters with a weaker 2D reconstruction network to encourage optimization of the microscope parameters, and later fix the microscope parameters to optimize a more powerful 3D reconstruction network alone to obtain higher quality reconstructions.

3 Results

Larval Zebrafish Dataset High resolution images of the whole brain of transgenic larval zebrafish expressing nuclear-restricted GCaMP6 calcium indicator in all neurons were imaged using a confocal microscope. These images are representative of brain-wide activity imaging. We train on 58 volumes (which we augment heavily) and test on 10 held-out volumes. For all experiments, we downsample the high resolution confocal data to $(1.0 \mu\text{m z}, 1.625 \mu\text{m y}, 1.625 \mu\text{m x})$. We created 4 datasets from these data called Type A, B, C, and D which correspond to imaging different fields of view cropped from the full dataset. Full specifications for these datasets are in Table 4 (Appendix A.2).

For Figure 2, we restrict the field of view to $(200 \mu\text{m z}, 416 \mu\text{m y}, 416 \mu\text{m x})$ with a tall cylinder cutout of diameter $193 \mu\text{m}$ and height $200 \mu\text{m}$ and image with 256×256 pixels on the simulated camera sensor. We call this setting of the data Type D. We also perform larger experiments with 512×512 pixels on the simulated camera sensor in Figure 3 and Table 2, with a field of view of $(250 \mu\text{m z}, 832 \mu\text{m y}, 832 \mu\text{m x})$ and three different settings for the data: Type A, Type B, and Type C. We explain these sample types in Section 3.3.

DiffuserCam Lensless Mirflickr Dataset We also test reconstruction performance on experimental computational photography data¹ from [12]. This is a dataset constructed by displaying RGB color

¹Publicly available: <https://waller-lab.github.io/LenslessLearning/dataset.html>

natural images from the MIRFlickr dataset on a monitor and then capturing diffused images by the DiffuserCam lensless camera. The dataset contains 24,000 pairs of DiffuserCam and ground truth images. The goal of the dataset is to learn to reconstruct the ground truth images from the diffused images. As in [12], we train on 23,000 paired diffused and ground truth images, and test on 999 held-out pairs of images.

3.1 Fourier convolutions outperform traditional deep networks for microscope optimization

Table 1: Quality of reconstructed volumes after optimizing microscope parameters to image Type D on 256×256 pixel camera (mean \pm s.e.m., $n = 10$)

Microscope	Reconstruction	$L_{\text{HNMSE}} \downarrow$	MS-SSIM \uparrow	PSNR \uparrow	Time \downarrow (s)
FourierNet2D	FourierNet3D	0.6409 ± 0.0213	0.955 ± 0.004	34.78 ± 0.88	0.71
FourierNet2D	FourierUNet3D	0.6325 ± 0.0222	0.956 ± 0.003	34.74 ± 0.83	1.37
FourierNet2D	UNet3D	0.7659 ± 0.0130	0.922 ± 0.008	30.06 ± 0.93	3.68
UNet2D	UNet3D	0.7120 ± 0.0160	0.913 ± 0.009	29.17 ± 1.13	3.68

We compare optimizing microscope parameters with two neural networks: 1) using our FourierNet with 2D convolutions (FourierNet2D) and 2) using a vanilla UNet with 2D convolutions (UNet2D). We train these microscopes and reconstruction networks on Type D, where samples are tall cylindrical cutouts of zebrafish with diameter $193 \mu\text{m}$ and height $200 \mu\text{m}$. Samples are imaged on a camera with 256×256 pixels (Figure 2). For the final reconstructions to be compared, we used more powerful networks with 3D convolutions and pre-trained microscope parameters as described in Section 3.2 and in more detail in Appendix A.3, A.4. FourierNet2D has 2 convolution layers, while UNet2D has 16 convolution layers. We include details on the reconstruction networks in Appendix A.3, A.4.

When looking at the resulting images in Figure 2, it is clear that the UNet microscope does not make sufficient use of all the pixels on the camera, producing only a single view of the sample. We see that the FourierNet microscope performs better than the UNet microscope for reconstruction in Figure 2, quantified in Table 1. Both reconstruction networks must reconstruct from images that have a compressed encoding of 3D information, but the FourierNet2D is clearly more effective than the UNet2D at optimizing this encoding.

3.2 Fourier convolutions outperform standard networks for volume reconstruction

We can determine which architecture is better for volume reconstruction by choosing fixed microscope parameters and varying the architecture. In Table 1, we compare results using a FourierNet with 3D convolutions (FourierNet3D), a FourierUNet with 3D convolutions (FourierUNet3D), and a vanilla UNet with 3D convolutions (UNet3D). We have already optimized microscope parameters with a weaker, faster network. We then train with these more powerful networks (with more parameters) to obtain higher reconstruction quality.

We include details on the reconstruction networks in Appendix A.3, A.4.

Table 2: Sample specific microscope parameter optimization across 3 different zebrafish sample types imaged with 512×512 pixel camera (mean PSNR (top), MS-SSIM (bottom) \pm s.e.m., $n = 10$). Green shaded regions show the regions of interest for each sample type, cropped from the full volume.

tested on	microscope parameters optimized for		
	Type A	Type B	Type C
Type A	49.75 ± 1.35	46.01 ± 1.33	42.63 ± 1.14
	0.998 ± 0.000	0.996 ± 0.001	0.992 ± 0.002
Type B	35.53 ± 1.41	37.28 ± 0.96	35.34 ± 1.16
	0.965 ± 0.004	0.972 ± 0.003	0.967 ± 0.003
Type C	30.87 ± 1.15	31.48 ± 0.93	33.79 ± 0.90
	0.912 ± 0.007	0.920 ± 0.006	0.935 ± 0.006

Reconstruction results in Table 1 compare normalized MSE L_{HNMSE} between the high pass filtered sample and high pass filtered reconstruction, the multiscale structural similarity MS – SSIM between the sample and reconstruction, and finally the peak signal-to-noise ratio PSNR. We also visualize reconstruction results for a volume in the head of a zebrafish in Figure 2. The best reconstruction networks are FourierNet3D and FourierUNet3D. The UNet3D reconstruction networks (using either

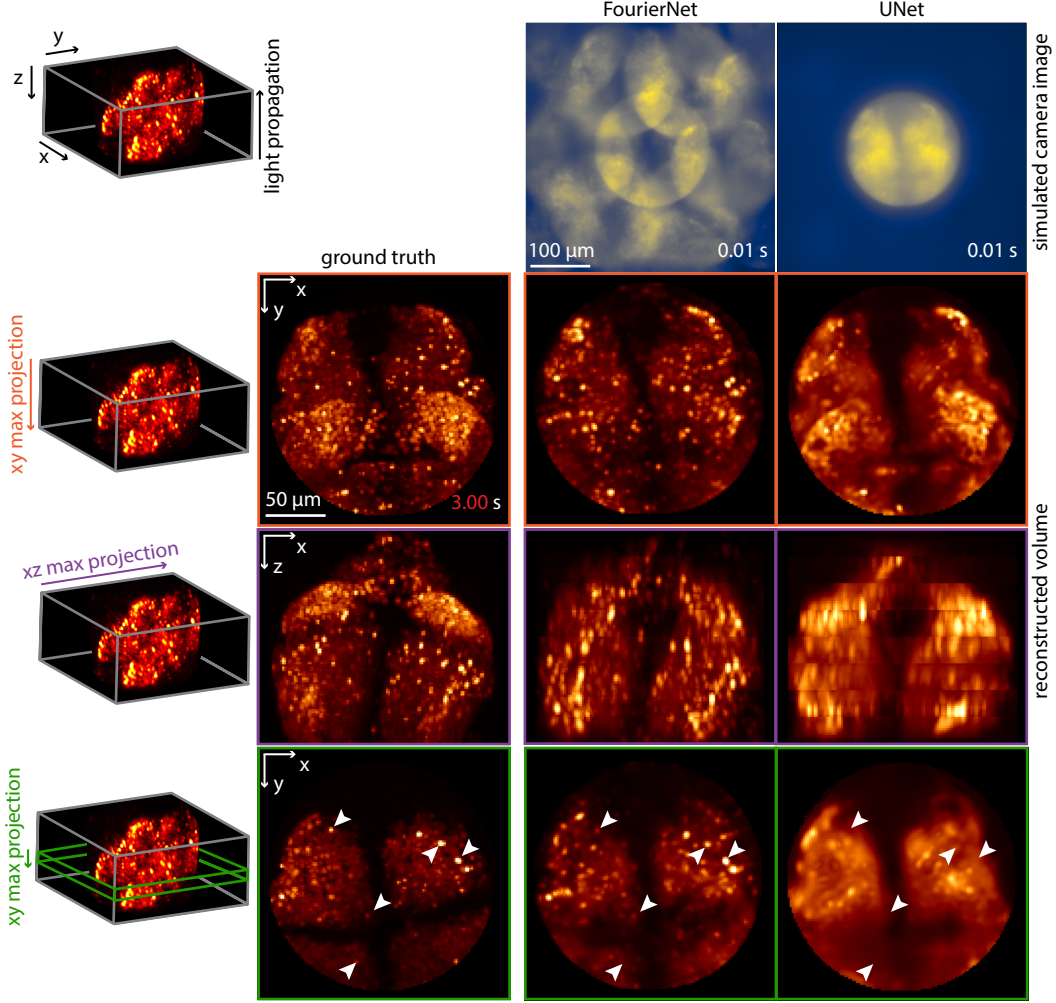


Figure 2: Comparison of reconstructions and simulated camera images of a Type D example obtained using our FourierNet (middle) versus UNet (right). Top row shows simulated 256×256 pixel camera images, with image capture time in bottom right. Colored arrows on the left column show axis of projection for images shown in each row (image border color matches corresponding projection arrow). In bottom row, white arrows point out individual neurons which are clearly visible for FourierNet but not for UNet. Ground truth has no corresponding camera image, because the 3D volume is imaged directly by confocal microscopy. FourierNet-based 3D snapshot microscopy can achieve high quality volume imaging at 100Hz with only minimal loss of resolution.

microscope) fall significantly behind the FourierNet3D/FourierUNet3D reconstruction networks in all metrics.

3.3 Microscope optimization depends on sample structure

In order to explore the effect of sample structure and size on the optimized microscope parameters and the resulting reconstruction performance, we optimized microscopes for three different sample types: 1) Type A, samples with a short cylinder cutout of $386 \mu\text{m}$ diameter and $25 \mu\text{m}$ height, 2) Type B, samples with a tall cylinder cutout of $386 \mu\text{m}$ diameter and $250 \mu\text{m}$ height, and 3) Type C, samples without any cutout of dimension $(250 \mu\text{m} z \times 832 \mu\text{m} y \times 832 \mu\text{m} x)$. Table 2 includes visualizations of these sample types. All sample types were imaged with 512×512 pixels on the simulated camera. We then tested the reconstruction performance on all combinations of optimized microscopes and samples, as shown in Figure 3 and Table 2. We include architecture details in Appendix A.3, A.5.

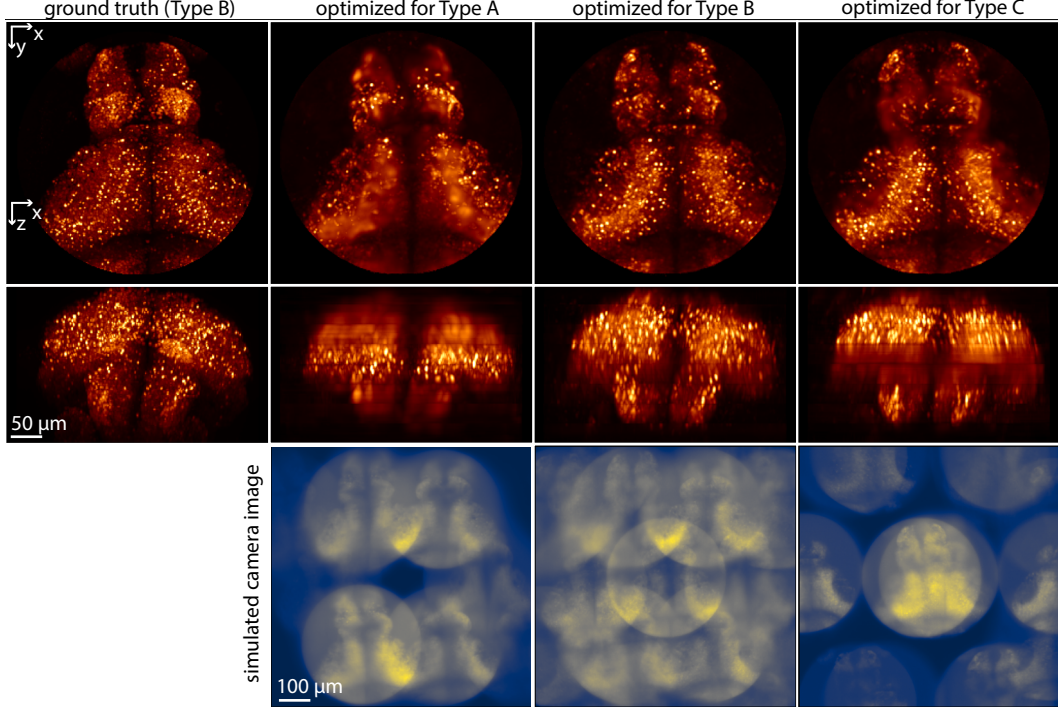


Figure 3: Reconstructed volumes resulting from imaging Type B samples by microscopes optimized for Type A, B, and C. Imaging Type B samples with microscope parameters optimized for Type B samples yields the best reconstructions. Top to bottom: xy max projection, xz max projection, simulated 512×512 camera image.

We see in Table 2 that for all sample types, the best performance is achieved using the microscope optimized for that particular sample. These results show that our optimization process produces designs that are optimal for a specific type of sample and not others.

3.4 Fourier convolutions outperform state-of-the-art learned methods on reconstructing natural images captured by the DiffuserCam lensless camera

Table 3: Quality of natural image reconstruction from lensless photography on the DiffuserCam Lensless Mirflickr Dataset (mean \pm s.e.m., $n = 999$). Superscripts denote loss function: ¹ MSE, ² MSE+LPIPS.

Method	MSE \downarrow ($\times 10^{-2}$)	LPIPS \downarrow	MS-SSIM \uparrow	PSNR \uparrow	Time \downarrow (ms)
FourierNet ¹	0.39 \pm 0.007	0.20 \pm 0.00	0.882 \pm 0.001	24.8 \pm 0.09	37.54
FourierNet ²	0.54 \pm 0.010	0.16 \pm 0.00	0.868 \pm 0.001	23.4 \pm 0.09	37.54
Le-ADMM-U ² [12]	0.75 \pm 0.021	0.19 \pm 0.00	0.865 \pm 0.002	22.1 \pm 0.09	59.01
UNet ² [12]	1.68 \pm 0.060	0.24 \pm 0.00	0.818 \pm 0.002	19.2 \pm 0.11	06.97

We compare our FourierNet architecture to the best learned method from [12] using an unrolled ADMM and a denoising UNet, as well as to a vanilla UNet from [12]. We include architecture details in Appendix A.3, A.6. We can see that both of our methods visually outperform the methods from [12] in Figure 4. We show in Table 3 that our methods outperform the others on all metrics. In [12], a combined loss using MSE and learned perceptual loss (LPIPS) is suggested to improve visual reconstruction quality. We observe in Table 3 that training our method on both MSE and LPIPS results in the lowest LPIPS loss across all methods, but does not offer better visual performance as seen in Figure 4.

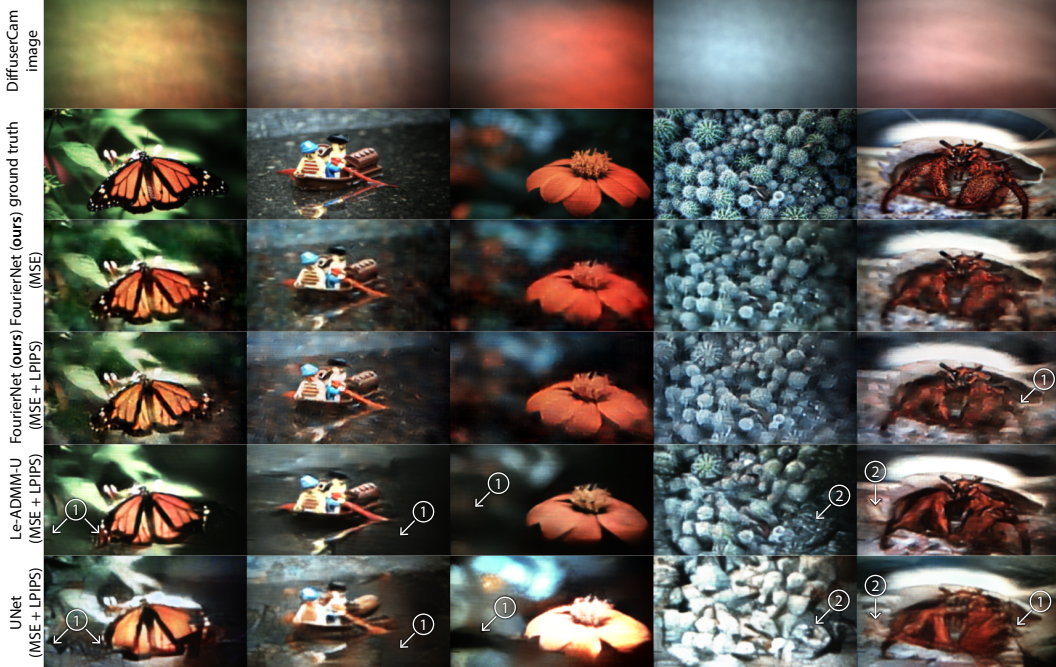


Figure 4: Comparisons of our method (second and third rows) to state-of-the-art learned reconstruction methods on lensless diffused images of natural scenes. Regions labeled ① indicate missing details, either resolution or textures in backgrounds. Regions labeled ② indicate hallucinated textures. Note that the previous state-of-the-art solutions [12] exhibit both issues more often compared to our models.

4 Discussion

Summary We have presented two new efficient global convolution architectures and applied these for the optimization of large field of view 3D snapshot microscope parameters where typical networks fail. Moreover, we have shown that these networks allow for superior reconstructions compared to other learned reconstruction methods — still providing the benefits of fast amortized inference and reconstruction times many orders of magnitude faster than traditional iterative reconstruction algorithms while also providing higher quality reconstructions due to the effective learning of structural priors of the class of samples being imaged. Generally, our global kernel architecture using Fourier convolutions could be applied to other problems where global computation of features is necessary (though we have focused on computational microscopy where such global mixing of information dominates).

Limitations Presently, imaging a different sample class (i.e. with different spatiotemporal statistics) will require retraining at least the reconstruction network, and ideally also the microscope parameters. Our autoencoder training style requires simulation of imaging with gradients, which can be memory expensive and limits the total field of view. Our training approach requires multi-GPU parallelization (described in Appendix A.2), and in practice we optimized microscopes using 8 RTX 8000 GPUs for the largest experiments, and 8 RTX 2080 Ti GPUs for the smaller experiments. Our Fourier convolution layers require a fixed input size to truly be global, though this could be addressed by resampling.

Broader Impact

Microscopy and photography with programmable optical elements has the potential to change how imaging is performed. End-to-end optimization of such optics can improve image quality but also enable multiplexed imaging not currently possible with standard optics. Our optical modeling library as well as our neural network architectures will be open-sourced and could enable new experiments in neuroscience through whole-brain imaging at an order of magnitude greater temporal resolution. Our training procedure does require long optimization periods with many GPUs, which poses a carbon footprint and barrier to usage compared to conventional microscopy.

Acknowledgments and Disclosure of Funding

We would like to thank William Bishop, Roman Vaxenburg, Janne Lappalainen, Nathan Klapoetke, Richard Xu, Lu Mi, Sridhama Prakhy, and Jinyao Yan for invaluable feedback and discussions. We thank Howard Hughes Medical Institute and a Simons Foundation grant (Simons Collaboration on the Global Brain, 542943SPI, Ahrens) for their funding. We also thank Huazhong University of Science and Technology and the China Scholarship Council for supporting the work of Zhenfei Jiao.

References

- [1] M. B. Ahrens, M. B. Orger, D. N. Robson, J. M. Li, and P. J. Keller, “Whole-brain functional imaging at cellular resolution using light-sheet microscopy,” *Nature Methods*, vol. 10, p. 413–420, May 2013.
- [2] Y. Mu, D. V. Bennett, M. Rubinov, S. Narayan, C.-T. Yang, M. Tanimoto, B. D. Mensh, L. L. Looger, and M. B. Ahrens, “Glia accumulate evidence that actions are futile and suppress unsuccessful behavior,” *Cell*, vol. 178, pp. 27–43.e19, Jun 2019.
- [3] W. Yang and R. Yuste, “In vivo imaging of neural activity,” *Nature Methods*, vol. 14, p. 349–359, Apr 2017.
- [4] M. Broxton, *Volume Reconstruction and Resolution Limits for Three Dimensional Snapshot Microscopy*. PhD thesis, Stanford University, Aug 2017.
- [5] N. Antipa, G. Kuo, R. Heckel, B. Mildenhall, E. Bostan, R. Ng, and L. Waller, “Diffusercam: lensless single-exposure 3d imaging,” *Optica*, vol. 5, p. 1–9, Jan 2018.
- [6] M. S. Asif, A. Ayremlou, A. Veeraraghavan, R. Baraniuk, and A. Sankaranarayanan, “Flatcam: Replacing lenses with masks and computation,” in *2015 IEEE International Conference on Computer Vision Workshop (ICCVW)*, p. 663–666, Dec 2015.
- [7] L. Cong, Z. Wang, Y. Chai, W. Hang, C. Shang, W. Yang, L. Bai, J. Du, K. Wang, and Q. Wen, “Rapid whole brain imaging of neural activity in freely behaving larval zebrafish (*danio rerio*),” *eLife*, vol. 6, p. e28158, Sep 2017.
- [8] Y. Hua, S. Nakamura, M. S. Asif, and A. C. Sankaranarayanan, “Sweepcam — depth-aware lensless imaging using programmable masks,” *IEEE Transactions on Pattern Analysis and Machine Intelligence*, vol. 42, p. 1606–1617, Jul 2020.
- [9] M. Levoy, R. Ng, A. Adams, M. Footer, and M. Horowitz, “Light field microscopy,” in *ACM SIGGRAPH 2006 Papers*, SIGGRAPH ’06, p. 924–934, Association for Computing Machinery, Jul 2006.
- [10] F. L. Liu, V. Madhavan, N. Antipa, G. Kuo, S. Kato, and L. Waller, “Single-shot 3d fluorescence microscopy with fourier diffusercam,” in *Biophotonics Congress: Optics in the Life Sciences Congress 2019 (BODA,BRAIN,NTM,OMA,OMP) (2019)*, paper NS2B.3, p. NS2B.3, Optical Society of America, Apr 2019.
- [11] F. Linda Liu, G. Kuo, N. Antipa, K. Yanny, and L. Waller, “Fourier diffuserscope: single-shot 3d fourier light field microscopy with a diffuser,” *Optics Express*, vol. 28, p. 28969, Sep 2020.
- [12] K. Monakhova, J. Yurtsever, G. Kuo, N. Antipa, K. Yanny, and L. Waller, “Learned reconstructions for practical mask-based lensless imaging,” *Optics Express*, vol. 27, p. 28075–28090, Sep 2019.
- [13] N. C. Pégard, H.-Y. Liu, N. Antipa, M. Gerlock, H. Adesnik, and L. Waller, “Compressive light-field microscopy for 3d neural activity recording,” *Optica*, vol. 3, p. 517–524, May 2016.
- [14] R. Prevedel, Y.-G. Yoon, M. Hoffmann, N. Pak, G. Wetzstein, S. Kato, T. Schrödel, R. Raskar, M. Zimmer, E. S. Boyden, and et al., “Simultaneous whole-animal 3d imaging of neuronal activity using light-field microscopy,” *Nature Methods*, vol. 11, p. 727–730, Jul 2014.
- [15] O. Skocek, T. Nöbauer, L. Weilguny, F. Martínez Traub, C. N. Xia, M. I. Molodtsov, A. Grama, M. Yamagata, D. Aharoni, D. D. Cox, and et al., “High-speed volumetric imaging of neuronal activity in freely moving rodents,” *Nature Methods*, vol. 15, p. 429–432, Jun 2018.
- [16] K. Yanny, N. Antipa, W. Liberti, S. Dehaeck, K. Monakhova, F. L. Liu, K. Shen, R. Ng, and L. Waller, “Miniscope3d: optimized single-shot miniature 3d fluorescence microscopy,” *Light: Science & Applications*, vol. 9, p. 171, Oct 2020.
- [17] K. Yanny, N. Antipa, R. Ng, L. Waller, and L. Waller, “Miniature 3d fluorescence microscope using random microlenses,” in *Biophotonics Congress: Optics in the Life Sciences Congress 2019 (BODA,BRAIN,NTM,OMA,OMP) (2019)*, paper BT3A.4, p. BT3A.4, Optical Society of America, Apr 2019.

- [18] E. Adelson and J. Wang, “Single lens stereo with a plenoptic camera,” *IEEE Transactions on Pattern Analysis and Machine Intelligence*, vol. 14, p. 99–106, Feb 1992.
- [19] L. Grosenick, M. Broxton, C. K. Kim, C. Liston, B. Poole, S. Yang, A. Andelman, E. Scharff, N. Cohen, O. Yizhar, and et al., “Identification of cellular-activity dynamics across large tissue volumes in the mammalian brain,” *bioRxiv*, p. 132688, May 2017.
- [20] L. B. Lesem, P. M. Hirsch, and J. A. Jordan, “The kinoform: A new wavefront reconstruction device,” *IBM Journal of Research and Development*, vol. 13, p. 150–155, Mar 1969.
- [21] J. N. Mait, “Understanding diffractive optic design in the scalar domain,” *JOSA A*, vol. 12, p. 2145–2158, Oct 1995.
- [22] F. Wyrowski, “Design theory of diffractive elements in the paraxial domain,” *JOSA A*, vol. 10, p. 1553–1561, Jul 1993.
- [23] L. B. Lucy, “An iterative technique for the rectification of observed distributions,” *The Astronomical Journal*, vol. 79, p. 745, Jun 1974.
- [24] W. H. Richardson, “Bayesian-based iterative method of image restoration*,” *JOSA*, vol. 62, p. 55–59, Jan 1972.
- [25] S. Boyd, N. Parikh, E. Chu, B. Peleato, and J. Eckstein, “Distributed optimization and statistical learning via the alternating direction method of multipliers,” *Foundations and Trends® in Machine Learning*, vol. 3, p. 1–122, Jan 2011.
- [26] S. Diamond, V. Sitzmann, F. Heide, and G. Wetzstein, “Unrolled optimization with deep priors,” *arXiv e-prints*, vol. 1705, p. arXiv:1705.08041, May 2017.
- [27] J. Dong, S. Roth, and B. Schiele, “Deep wiener deconvolution: Wiener meets deep learning for image deblurring,” *Advances in Neural Information Processing Systems*, vol. 33, p. 1048–1059, 2020.
- [28] Z. Wang, L. Zhu, H. Zhang, G. Li, C. Yi, Y. Li, Y. Yang, Y. Ding, M. Zhen, S. Gao, and et al., “Real-time volumetric reconstruction of biological dynamics with light-field microscopy and deep learning,” *Nature Methods*, p. 1–6, Feb 2021.
- [29] E. Nehme, D. Freedman, R. Gordon, B. Ferdman, L. E. Weiss, O. Alalouf, T. Naor, R. Orange, T. Michaeli, and Y. Shechtman, “Deepstorm3d: dense 3d localization microscopy and psf design by deep learning,” *Nature Methods*, vol. 17, p. 734–740, Jul 2020.
- [30] J. Goodman, *Introduction to Fourier Optics*. Macmillan Learning, 4 ed., 2017.
- [31] O. Ronneberger, P. Fischer, and T. Brox, “U-net: Convolutional networks for biomedical image segmentation,” in *Medical Image Computing and Computer-Assisted Intervention – MICCAI 2015* (N. Navab, J. Hornegger, W. M. Wells, and A. F. Frangi, eds.), Lecture Notes in Computer Science, p. 234–241, Springer International Publishing, 2015.
- [32] A. V. Oppenheim and A. S. Willsky, *Signals and Systems: Pearson New International Edition*. Pearson Education Limited, Jul 2013. Google-Books-ID: ut9oAQAAQAAJ.
- [33] M. Mathieu, M. Henaff, and Y. LeCun, “Fast training of convolutional networks through ffts,” *arXiv:1312.5851 [cs]*, Mar 2014. arXiv: 1312.5851.
- [34] N. Vasilache, J. Johnson, M. Mathieu, S. Chintala, S. Piantino, and Y. LeCun, “Fast convolutional nets with fbfft: A gpu performance evaluation,” *arXiv:1412.7580 [cs]*, Apr 2015. arXiv: 1412.7580.
- [35] S. Ioffe and C. Szegedy, “Batch normalization: Accelerating deep network training by reducing internal covariate shift,” *arXiv:1502.03167 [cs]*, Mar 2015. arXiv: 1502.03167.
- [36] D. Ulyanov, A. Vedaldi, and V. Lempitsky, “Instance normalization: The missing ingredient for fast stylization,” *arXiv:1607.08022 [cs]*, Nov 2017. arXiv: 1607.08022.

A Appendix

A.1 Forward simulation of programmable 3D snapshot microscope

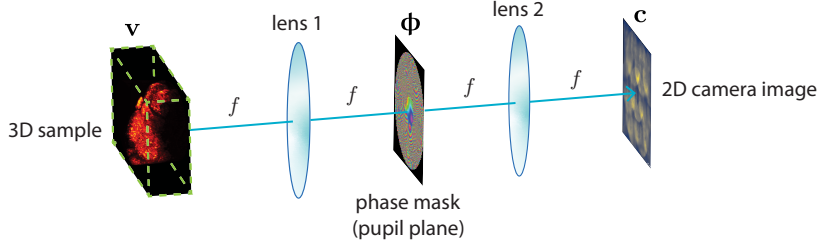


Figure 5: Diagram of a $4f$ optical model that is the basis for our simulated microscope M_ϕ , showing the Fourier plane in which we have the programmable and trainable 2D phase mask ϕ .

Here we describe our wave optics simulation of the microscope M_ϕ , which we model as a $4f$ system [30]. The $4f$ optical system consists of two lenses, the first spaced one focal length from the object plane and the second spaced one focal length away from one focal length beyond the first lens (Figure 5). In between these two lenses, we can place a phase mask to manipulate the light field before passing through the second lens and forming an image on the camera sensor.

We are concerned here with fluorescence microscopy, meaning that the sources of light that we image are individual fluorescent molecules, which we can model as point emitters. Because these molecules emit incoherent light, the camera sensor in effect sums the contributions of each point emitter. In order to model such an imaging system, we first need to address modeling a single point emitter's image on the camera.

We can analytically calculate the complex-valued light field one focal length after the first lens (which we call the pupil plane) due to a point source centered at some plane z (where z is a distance from the object plane $z = 0$). If the point source were centered ($x = 0, y = 0$) in the object focal plane $z = 0$, we would have a plane wave at the pupil plane, but for the more general case of a point source at an arbitrary plane z relative to the object plane $z = 0$, we can analytically calculate the complex-valued light field entering the pupil plane:

$$u_{\text{point}}(\mathbf{k}; z) = \exp \left[i2\pi z \sqrt{\left(\frac{n}{\lambda}\right)^2 - \|\mathbf{k}\|_2^2} \right] \quad (9)$$

where u_{point} is the incoming light field entering the pupil due to a point source centered in the plane at z , $\mathbf{k} \in \mathbb{R}^2$ denotes frequency space coordinates of the light field in the pupil plane, n is the refractive index, and λ is the wavelength of light [30].

In this pupil plane, we can then apply a phase mask ϕ to the light field, which is modeled as a multiplication of $u_{\text{point}}(\mathbf{k}; z)$ and $e^{i\phi(\mathbf{k})}$, the complex phase of the pupil function. The light field exiting the pupil is therefore described by

$$u_{\text{pupil}}(\mathbf{k}; z) = u_{\text{point}}(\mathbf{k}; z)p(\mathbf{k}) \quad (10)$$

where $p(\mathbf{k})$ is the pupil function, composed of an amplitude $a(\mathbf{k})$ and phase $\phi(\mathbf{k})$:

$$p(\mathbf{k}) = a(\mathbf{k})e^{i\phi(\mathbf{k})} \quad (11)$$

$$a(\mathbf{k}) = \begin{cases} 1 & \|\mathbf{k}\|_2 \leq \frac{\text{NA}}{\lambda} \\ 0 & \|\mathbf{k}\|_2 > \frac{\text{NA}}{\lambda} \end{cases} \quad (12)$$

where NA is the numerical aperture of the lens [30].

The light field at the camera plane can then be described by a Fourier transform [30]:

$$\mathbf{u}_{\text{camera}} = \mathcal{F} \{ \mathbf{u}_{\text{pupil}} \} \quad (13)$$

The camera measures the intensity of this complex field:

$$s(\mathbf{x}; z) = |u_{\text{camera}}(\mathbf{x}; z)|^2 \quad (14)$$

where $\mathbf{x} \in \mathbb{R}^2$ denotes spatial coordinates in the camera plane [30].

We can call this intensity s the point response function (PRF). If the shape of the PRF is translationally equivariant in \mathbf{x} , meaning that moving a point source in-plane creates the same field at the camera, just shifted by the corresponding amount, then we call this PRF a point spread function (PSF). Note that moving the point source in z will not give the same shape, which allows our system to encode depth information through the PSF [4].

In order to avoid edge effects during imaging, we simulate the PSF at a larger field of view, then crop and taper the edges of the PSF:

$$\mathbf{s}_{\text{taper}} = \text{crop}[\mathbf{s}] \odot \mathbf{t} \quad (15)$$

where \mathbf{t} is a taper function created by taking the sigmoid of a distance transform divided by a width factor controlling how quickly the taper goes to 0 at the edges and \odot denotes elementwise multiplication. We intentionally simulate a larger field of view than the sample in order to avoid edge artifacts. The purpose of the $\text{crop}[\cdot]$ is to cut the PSF to the correct field of view. The purpose of the tapering is to remove artifacts at the edges of the cropped PSF. After we compute this cropped and tapered PSF, we also downsample $\mathbf{s}_{\text{taper}}$ to the size of the data \mathbf{v} in order to save memory.

Imaging is equivalent to the convolution of the incoming light field volume intensity \mathbf{v} and the cropped and tapered PSF $\mathbf{s}_{\text{taper}}$ for a given plane. At the camera plane, the light field intensity is measured by the camera sensor. Therefore, we can describe the forward model as the following convolution and integral over planes:

$$\mu_{\mathbf{c}}(\mathbf{x}) = \iint v(\boldsymbol{\tau}_{\mathbf{x}}; z) s_{\text{taper}}(\mathbf{x} - \boldsymbol{\tau}_{\mathbf{x}}; z) d\boldsymbol{\tau}_{\mathbf{x}} dz \quad (16)$$

In practice, we discretize the convolution and also sum over a discrete number of planes. We then model shot noise of the camera sensor to produce the final image \mathbf{c} , for which the appropriate model is sampling from a Poisson distribution with a mean of $\mu_{\mathbf{c}}$ [30]:

$$\mathbf{c} \sim \text{Poisson}(\mu_{\mathbf{c}}) \quad (17)$$

However, because we cannot use the reparameterization trick to take pathwise derivatives through the discrete Poisson distribution, we instead approximate the noise model with a rectified Gaussian distribution:

$$\epsilon \sim \mathcal{N}(0, 1) \quad (18)$$

$$\mathbf{c} \approx \max([\mu_{\mathbf{c}} + \sqrt{\mu_{\mathbf{c}}}\epsilon], 0) \quad (19)$$

A.2 Training PSFs and volume reconstruction networks

Given a simulation of imaging, we can define two modes of autoencoder training: (1) jointly training the phase mask parameters $\boldsymbol{\phi}$ and weak reconstruction networks in order to learn a good PSF for a particular class of samples (i.e. samples with the same spatiotemporal statistics), and (2) training a stronger reconstruction network only with a fixed, pre-trained $\boldsymbol{\phi}$.

Definition of terms For both cases of training, the general framework is to simulate imaging using confocal volumes of pan-neuronal labeled larval zebrafish, reconstruct from the simulated image, then update the reconstruction network and, if desired, the microscope parameters. We will define the microscope parameters as $\boldsymbol{\phi}$ and the reconstruction network parameters as $\boldsymbol{\theta}$ for any reconstruction network $\mathbf{R}_{\boldsymbol{\theta}}(\mathbf{c})$ where $\mathbf{R}_{\boldsymbol{\theta}}$ maps 2D images to 3D volume reconstructions. For our training algorithms listed below, we also define: \mathbf{D} our **dataset**, \mathbf{v} a **ground truth volume**, $\hat{\mathbf{v}}$ a **reconstructed volume**, L a computed **loss**, z_s a list of z plane indices that will be imaged/reconstructed, $\alpha_{\boldsymbol{\phi}}$ the learning rate for the microscope parameters, $\alpha_{\boldsymbol{\theta}}$ the learning rate for the reconstruction network parameters, and β the weight of the non-high pass filtered component of the loss. When selecting a random ground truth volume, we also perform random shift, rotation, flip, and brightness augmentations.

Microscope simulation parameters When simulating the zebrafish imaging, we use a wavelength of $0.532 \mu\text{m}$ for all simulations. The NA of our microscope is 0.8. The refractive index n is 1.33. We

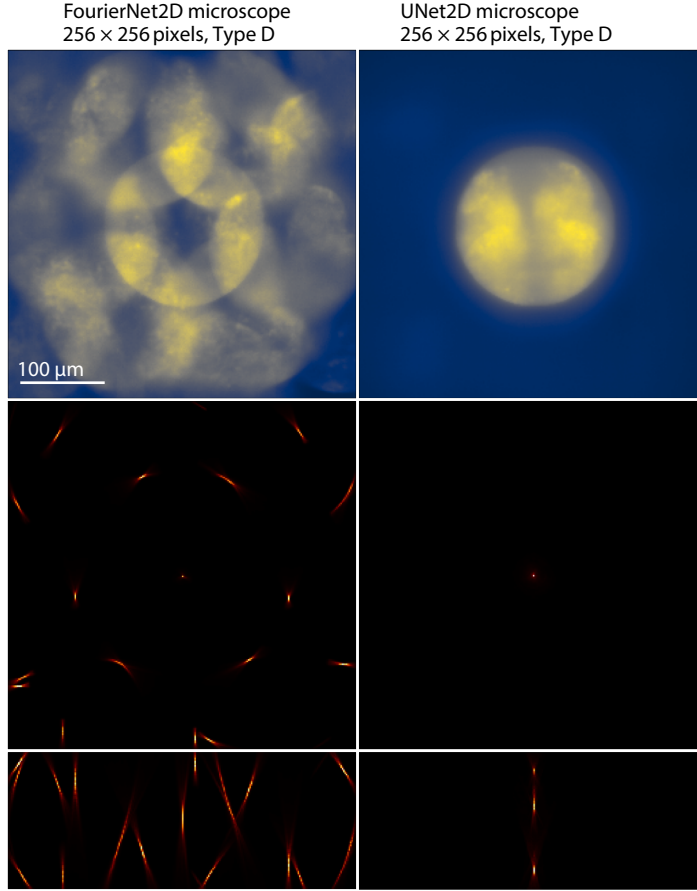


Figure 6: FourierNet successfully optimizes a PSF to image and reconstruct Type D where UNet fails. The FourierNet learned to produce multiple pencils in its PSF, which create multiple views of the sample in the camera image. UNet learned only a single pencil and fails to utilize the majority of pixels in the camera image to encode views of the sample. Top row shows simulated camera image of a Type D example, middle row shows xy max projection of the PSF, and bottom row shows xz max projection of the PSF.

downsample all volumes to $(1.0 \mu\text{m} z, 1.625 \mu\text{m} y, 1.625 \mu\text{m} x)$. We use a taper width of 5 for all simulations, and simulate the PSF at 50% larger dimensions in x and y. The resolution of the camera (for all zebrafish datasets) is also $(1.625 \mu\text{m} y, 1.625 \mu\text{m} x)$.

Initialization of ϕ For Type A, B, and D, we initialize ϕ to produce a PSF consisting of 6 pencil beams at different locations throughout the depth of the volume, with the centers of these beams arranged in a hexagonal pattern in x and y. Because our optimizations generally find PSFs with many pencils, we find that initializing with such a pattern helps to converge to a more optimal PSF (data not shown).

For Type C, we instead initialize with a single helix spanning the depth of the volume (the ‘‘Potato Chip’’ from [4]), which seems to find a local minimum for ϕ that produces a PSF with more pencils (and therefore views in the camera image).

Data settings and augmentation for Type A, B, C, D Using our total 58 training zebrafish volumes and 10 testing zebrafish volumes (imaged through confocal microscopy), we crop in four different ways to create four different datasets. For training volumes, we crop from random locations from each volume as a form of augmentation. For testing, we crop from the same location. Physically, these crops correspond to either placing a circular aperture before light hits the $4f$ system or changing the illumination thickness in z , because samples would be illuminated from the side in a real implementation of this microscope. We model these by cropping cylinders (or cubes if there is no

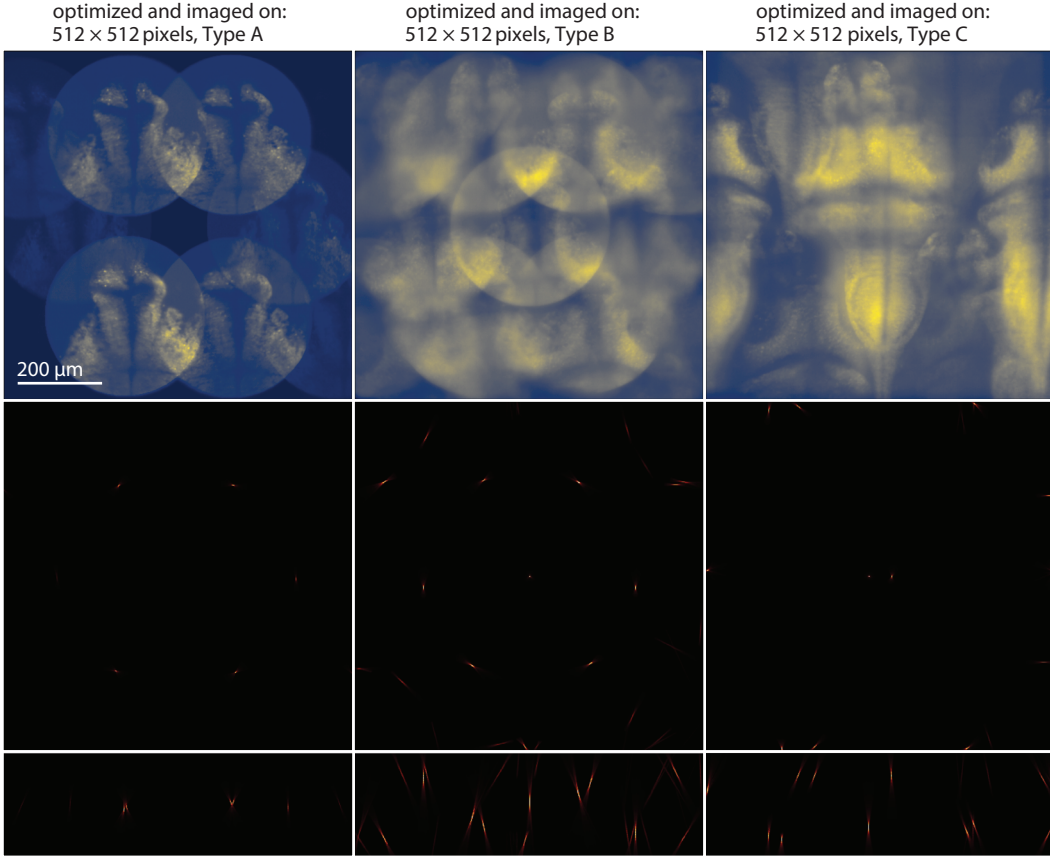


Figure 7: Optimizing PSFs for different samples result in PSFs tailored to each sample. Note that PSF optimized for Type A (left) has pencils with a span in z that matches Type A. PSF optimized for Type B (middle) has pencils that span the entire z depth. PSF optimized for Type C (right) has pencils spread farther apart to account for the larger sample. Top row shows simulated camera image of a Type A, B, or C example respectively, middle row shows xy max projection of the PSF, and bottom row shows xz max projection of the PSF.

aperture) of different diameters and heights. We show details for all types Type A, B, C, D in Table 4, where the diameter of the cylinder is labeled “Aperture Diameter” and the illumination thickness is labeled “Height”.

We augment our volumes during training by taking random locations from these volumes, randomly rotating the volumes, randomly flipping the volumes, and also randomly rotating in pitch, yaw, and roll. Most importantly, we also randomly scale the brightness of our samples and add random background levels which serve to adjust the signal-to-noise ratio (SNR) of the resulting simulated images. The only exception to these augmentations is Type C, where we set all the volumes to the same in-plane vertical orientation (while still applying rotation augmentations in pitch and roll).

Table 4: Specifications of all zebrafish datasets Type A, B, C, D for reconstruction

Dataset	Camera (px)	Height (planes)	Span (z, y, x) (μm)	Aperture Diameter (μm)
Type A	512×512	12	(25, 832, 832)	386
Type B	512×512	128	(250, 832, 832)	386
Type C	512×512	128	(250, 832, 832)	-
Type D	256×256	96	(200, 416, 416)	193

Parallelizing imaging and reconstruction Furthermore, because this simulation can become too expensive in memory to fit on a single device, we generally perform the simulation, reconstruction, and loss calculation in parallel for both training modes. Therefore, any variable that has a $_s$ subscript refers to a list of chunks of that variable that will be run on each device. A j superscript indicates a particular chunk for GPU j . For example z_s is a list of plane indices to be imaged/reconstructed, and z_s^j is the j^{th} chunk of plane indices that will be imaged/reconstructed on GPU j . We denote `parallel` for any operations that are performed in parallel and `scatter` for splitting data into chunks and spreading across multiple GPUs. Imaging can be cleanly parallelized: chunks of a PSF and sample can be partially imaged on multiple GPUs independently because the convolution occurs per plane, then finally all partial images can be summed together onto a single GPU. The reconstructions can similarly take the final image and reconstruct partial chunks (as well as calculate losses on partial chunks) of the volume independently per device. We implicitly gather data to the same GPU when computing sums (\sum) or means (\mathbb{E}). The functions `parallel image` and `compute PSF` follow the definitions above in equations 16 and 14. In the algorithms shown here, `parallel image` applies the same convolution described above in equation 16.

Sparse gradients and downsampling We additionally support training and reconstructing only some of the planes for imaging and potentially a different partial group of planes during reconstruction, as a way to sparsely compute gradients for optimization of θ_m and save memory. The planes not imaged with gradients can still contribute to the image (without their gradients being tracked) in order to make the problem more difficult for the reconstruction network. Over multiple iterations, this can become equivalent to the more expensive densely computed gradient method, essentially trading training time for memory. An additional memory saving measure not written in the algorithms is to compute the PSF at a high resolution, then downsample the PSF using a 2D sum pool to preserve total energy in order to reduce memory usage when performing the imaging and reconstruction. We denote **with no gradient tracking** to show an operation without gradients.

A.3 Implementation details

Fourier convolution details Our implementation of the Fourier convolution uses complex number weights, implemented as two real numbers. Furthermore, in order to prevent the convolution from wrapping around the edges, we have to pad the input to double the size. The size of the weight must match the size of this padded input. This means that the number of parameters for our Fourier convolution implementation is $8 \times$ the number of parameters required for a global kernel in a spatial convolution (though the Fourier convolution is significantly faster).

Common network details All convolutions (including Fourier convolutions) use “same” padding. For FourierUNets and vanilla UNets, downsampling and upsampling is performed only in the x and y dimensions (we do not downsample or upsample in z because there could potentially not be enough planes to do so). We train all networks using the ADAM optimizer with all default PyTorch parameters except the learning rate, which we always set to 10^{-4} for the reconstruction network parameters θ and 10^{-2} for the phase mask parameters Φ .

Normalization We use **input scaling** during both training and inference in order to normalize out differences in the brightness of the image and prevent instabilities in our gradients. This means we divide out the median value of the input (scaled by some factor in order to bring the loss to a reasonable range) and then undo this scaling after the output of the network. This effectively linearizes our reconstruction networks, meaning a scaling of the image sent to the network will exactly scale the output by that value. We also find this is a more effective and simpler alternative to using a BatchNorm on our inputs. We continue to use BatchNorm between our convolution layers within the reconstruction network [35], which is effectively InstanceNorm in our case where batch size is 1 [36].

Planewise network training logic When we train PSFs by optimizing Φ , we train separate reconstruction networks per plane. This allows us to flexibly compute sparse gradients across different planes from iteration to iteration, as described in Appendix A.2. In order to do this, we create placeholder networks on any number of GPUs, then copy the parameters stored on CPU for each plane’s reconstruction network to a network on the GPU as needed during a forward pass. After calculating an update with the optimizer, we copy the parameter values back to the corresponding parameter on CPU.

Algorithm 1: Parallel PSF engineering by joint training of reconstruction network and phase mask. Microscope M_ϕ parameters are ϕ , reconstruction network R_θ parameters are θ , dataset is D , learning rates for ϕ and θ are α_ϕ and α_θ respectively, plane indices to image and reconstruct from z_s , and weight for L_{NMSE} is β .

Input: $M_\phi, \phi, \alpha_\phi, R_\theta, \theta, \alpha_\theta, D, z_s, \beta$

```

1 for  $v \in D$  do
2   // select plane indices to be imaged with and without gradients
3    $z_{s,\text{gradient}}, z_{s,\text{no gradient}} \leftarrow \text{select planes}(z_s)$ 
4   // move sample planes to be imaged with gradients to multiple GPUs
5    $v_{s,\text{gradient}} \leftarrow \text{scatter}(v, z_{s,\text{gradient}})$ 
6   // move sample planes to be imaged without gradients to multiple GPUs
7    $v_{s,\text{no gradient}} \leftarrow \text{scatter}(v, z_{s,\text{no gradient}})$ 
8   // compute PSF with gradients on multiple GPUs
9    $s_{s,\text{gradient}} \leftarrow \text{parallel}(\text{compute PSF}(M_\phi, z_s^j) \text{ for } z_s^j \text{ in } z_{s,\text{gradient}})$ 
10  // compute partial image with gradients on multiple GPUs
11   $c_{\text{gradient}} \leftarrow \text{parallel image}(s_{s,\text{gradient}}, v_{s,\text{gradient}})$ 
12  // compute PSF without gradients on multiple GPUs
13  with no gradient tracking
14  |  $s_{s,\text{no gradient}} \leftarrow \text{parallel}(\text{compute PSF}(M_\phi, z_s^j) \text{ for } z_s^j \text{ in } z_{s,\text{no gradient}})$ 
15  end
16  // compute partial image without gradients on multiple GPUs
17  with no gradient tracking
18  |  $c_{\text{no gradient}} \leftarrow \text{parallel image}(s_{s,\text{no gradient}}, v_{s,\text{no gradient}})$ 
19  end
20  // compute full image by summing partial images onto one GPU
21   $c \leftarrow \sum[c_{\text{gradient}}, c_{\text{no gradient}}]$ 
22  // select plane indices to be reconstructed
23   $z_{s,\text{reconstruct}} \leftarrow \text{select planes}(z_s)$ 
24  // move sample planes that will be reconstructed to multiple GPUs
25   $v_{s,\text{reconstruct}} \leftarrow \text{scatter}(v, z_{s,\text{reconstruct}})$ 
26  // compute mean of high passed sample for loss normalization
27   $\mu_H(v) \leftarrow \mathbb{E}(H(v_{s,\text{reconstruct}})^2)$ 
28  // compute mean of sample for loss normalization
29   $\mu_v \leftarrow \mathbb{E}(v_{s,\text{reconstruct}}^2)$ 
30  // move reconstruction networks to multiple GPUs
31   $R_{\theta,s} \leftarrow \text{scatter}(R_\theta)$ 
32  // compute reconstruction and loss on multiple GPUs
33   $L \leftarrow \text{parallel reconstruct/loss}(c, v_{s,\text{reconstruct}}, R_{\theta,s}, \mu_H(v), \mu_v, \beta)$ 
34  // compute gradients for all parameters
35   $g_\theta \leftarrow \nabla_\theta L$ 
36   $g_\phi \leftarrow \nabla_\phi L$ 
37  // update all parameters
38   $\theta \leftarrow \text{ADAM}(\alpha_\theta, \theta, g_\theta)$ 
39   $\phi \leftarrow \text{ADAM}(\alpha_\phi, \phi, g_\phi)$ 
40 end

```

A.4 Details for Fourier convolutions outperform standard networks for volume reconstruction

For our experiments in Sections 3.1 and 3.2, we use 40 planes at $5\mu\text{m}$ resolution in z and therefore 40 reconstruction networks to train PSFs. When training reconstruction networks only to produce the higher quality reconstructions, we use 96 planes at $1\mu\text{m}$ resolution in z (chosen so that the planes actually span $200\mu\text{m}$ in z). We train in both settings without any sparse planewise gradients, meaning we image and reconstruct all 40 or all 96 planes, respectively. We show details of all datasets used for training reconstructions in Table 4.

Algorithm 2: Parallel training a reconstruction network given a pre-trained phase mask. Microscope M_ϕ parameters are ϕ (phase mask), reconstruction network R_θ parameters are θ , dataset is D , learning rates for ϕ and θ are α_ϕ and α_θ respectively, plane indices to image and reconstruct from are z_s , and weight for L_{NMSE} is β .

```

Input:  $M_\phi, \phi, \alpha_\phi, R_\theta, \theta, \alpha_\theta, D, z_s, \beta$ 
// compute PSF without gradients on multiple GPUs
1 with no gradient tracking
2 |  $s_{\text{no gradient}} \leftarrow \text{parallel}(\text{compute PSF}(M_\phi, z_s^j) \text{ for } z_s^j \text{ in } z_s)$ 
3 end
4 for  $v \in D$  do
| // select plane indices to be imaged without gradients
5  $z_{s, \text{no gradient}} \leftarrow \text{select planes}(z_s)$ 
| // move sample planes to be imaged without gradients to multiple GPUs
6  $v_{s, \text{no gradient}} \leftarrow \text{scatter}(v, z_{s, \text{no gradient}})$ 
| // move necessary PSF planes to multiple GPUs
7  $s_{s, \text{no gradient}} \leftarrow \text{scatter}(s_{\text{no gradient}}, z_{s, \text{no gradient}})$ 
| // compute image without gradients on multiple GPUs
8 with no gradient tracking
9 |  $c \leftarrow \text{parallel image}(s_{s, \text{no gradient}}, v_{s, \text{no gradient}})$ 
10 end
| // select plane indices to be reconstructed
11  $z_{s, \text{reconstruct}} \leftarrow \text{select planes}(z_s)$ 
| // move sample planes that will be reconstructed to multiple GPUs
12  $v_{s, \text{reconstruct}} \leftarrow \text{scatter}(v, z_{s, \text{reconstruct}})$ 
| // compute mean of high passed sample for loss normalization
13  $\mu_{H(v)} \leftarrow \mathbb{E}[H(v_{s, \text{reconstruct}})^2]$ 
| // compute mean of sample for loss normalization
14  $\mu_v \leftarrow \mathbb{E}[v_{s, \text{reconstruct}}^2]$ 
| // move reconstruction networks to multiple GPUs
15  $R_{\theta, s} \leftarrow \text{scatter}(R_\theta)$ 
| // compute reconstruction and loss on multiple GPUs
16  $L \leftarrow \text{parallel reconstruct/loss}(c, v_{s, \text{reconstruct}}, R_{\theta, s}, \mu_{H(v)}, \mu_v, \beta)$ 
| // compute gradients for reconstruction networks only
17  $g_\theta \leftarrow \nabla_\theta L$ 
| // update reconstruction network parameters only
18  $\theta \leftarrow \text{ADAM}(\alpha_\theta, \theta, g_\theta)$ 
19 end

```

Algorithm 3: Parallel imaging. PSF planes on multiple GPUs are s_s , sample planes on multiple GPUs to be imaged are v_s .

```

Input :  $s_s, v_s$ 
Output :  $c$ 
// compute images in parallel on multiple GPUs, then sum to single GPU
1  $c \leftarrow \sum[\text{parallel}(\text{convolve}(s_s^j, v_s^j) \text{ for } (s_s^j, v_s^j) \text{ in } (s_s, v_s))]$ 
2 return  $c$ 

```

We show the details of our FourierNet2D architecture for training PSFs in Table 7 and our FourierNet3D architecture for training reconstruction networks in Table 8. We also show details for training times for both training PSFs and for training more powerful reconstruction networks in Table 5. We trained all networks for Type D for the same number of iterations (more than necessary for PSFs to meaningfully converge)².

²Training times are approximate, and actual total time was longer due to checkpointing/snapshotting/validation of data and/or differences in load on the clusters being used.

Algorithm 4: Parallel reconstruction/loss calculation. Camera image is \mathbf{c} , sample planes on multiple GPUs are \mathbf{v}_s , reconstruction networks on multiple GPUs are $\mathbf{R}_{\theta,s}$, mean for L_{HNMSE} normalization is $\mu_{H(\mathbf{v})}$, mean for L_{NMSE} normalization is $\mu_{\mathbf{v}}$, and weight for L_{NMSE} is β .

Input : $\mathbf{c}, \mathbf{v}_s, \mathbf{R}_{\theta,s}, \mu_{H(\mathbf{v})}, \mu_{\mathbf{v}}, \beta$
Output : L
 // compute reconstruction and loss in parallel on multiple GPUs
 1 $\hat{\mathbf{v}}_s \leftarrow \text{concatenate}(\text{parallel}(\mathbf{R}_s^j(\mathbf{c}) \text{ for } \mathbf{R}_s^j \text{ in } \mathbf{R}_{\theta,s}))$
 2 $L_s \leftarrow \text{parallel}(\frac{\mathbb{E}[(H(\mathbf{v}_s^j) - H(\hat{\mathbf{v}}_s^j))^2]}{\mu_{H(\mathbf{v})}} + \beta \frac{\mathbb{E}[(\mathbf{v}_s^j - \hat{\mathbf{v}}_s^j)^2]}{\mu_{\mathbf{v}}}) \text{ for } (\hat{\mathbf{v}}_s^j, \mathbf{v}_s^j) \text{ in } (\hat{\mathbf{v}}_s, \mathbf{v}_s))$
 // compute mean of scattered losses on single GPU
 3 $L \leftarrow \mathbb{E}[L_s]$
 4 **return** L

Table 5: Type D experiment training times

Network	Parameters	# train steps	Train step time (s)	Total time (h)
FourierNet2D	Θ, Φ	10^6	~ 0.8	~ 222
FourierNet3D	Θ	10^6	~ 0.4	~ 111
FourierUNet3D	Θ	10^6	~ 0.7	~ 194
UNet2D	Θ, Φ	10^6	~ 1.3	~ 361
UNet3D	Θ	10^6	~ 0.8	~ 222

Table 6: Type A, B, C experiment training times

Network	Parameters	Zebrafish	# train steps	Train step time (s)	Total time (h)
FourierNet2D	Θ, Φ	A	5.8×10^5	~ 1.1	~ 177
FourierNet3D	Θ (fixed Φ for A)	A	$\sim 2.6 \times 10^5$	~ 1.6	~ 116
FourierNet3D	Θ (fixed Φ for A)	B	$\sim 1.3 \times 10^5$	~ 1.6	~ 58
FourierNet3D	Θ (fixed Φ for A)	C	$\sim 1.3 \times 10^5$	~ 1.6	~ 58
FourierNet2D	Θ, Φ	B	5.8×10^5	~ 1.1	~ 177
FourierNet3D	Θ (fixed Φ for B)	A	$\sim 1.2 \times 10^5$	~ 1.6	~ 53
FourierNet3D	Θ (fixed Φ for B)	B	10^6	~ 1.6	~ 444
FourierNet3D	Θ (fixed Φ for B)	C	$\sim 5.0 \times 10^5$	~ 1.6	~ 222
FourierNet2D	Θ, Φ	C	5.8×10^5	~ 1.1	~ 177
FourierNet3D	Θ (fixed Φ for C)	A	$\sim 3.4 \times 10^5$	~ 1.6	~ 151
FourierNet3D	Θ (fixed Φ for C)	B	$\sim 3.4 \times 10^5$	~ 1.6	~ 151
FourierNet3D	Θ (fixed Φ for C)	C	$\sim 3.7 \times 10^5$	~ 1.6	~ 164

Table 7: FourierNet2D detailed architecture (1 per plane)

Layer type	Kernel size	Stride	Notes	Shape (C, D, H, W)
InputScaling	-	-	scale: 0.01	(1, 1, 256, 256)
FourierConv2D	(256, 256)	(2, 2)	-	(8, 1, 256, 256)
LeakyReLU	-	-	slope: -0.01	(8, 1, 256, 256)
BatchNorm2D	-	-	-	(8, 1, 256, 256)
Conv2D	(11, 11)	(1, 1)	-	(1, 1, 256, 256)
ReLU	-	-	-	(1, 1, 256, 256)
InputRescaling	-	-	scale: 0.01	(1, 1, 256, 256)

The architecture of FourierUNet3D is 4 scales, with a cropping factor of 2 per scale in the encoding path and an upsampling factor of 2 in the decoding path. For each scale, we perform a Fourier convolution in the encoding path producing 480 feature maps, which are concatenated with the incoming feature maps of the decoding convolutions at the corresponding scale (just as in a normal

Table 8: FourierNet3D detailed architecture (8 GPUs)

Layer type	Kernel size	Stride	Notes	Shape (C, D, H, W)
InputScaling	-	-	scale: 0.01	(1, 1, 256, 256)
FourierConv2D	(256, 256)	(2, 2)	-	(60, 1, 256, 256)
LeakyReLU	-	-	slope: -0.01	(60, 1, 256, 256)
BatchNorm2D	-	-	-	(60, 1, 256, 256)
Reshape2D3D	-	-	-	(5, 12, 256, 256)
Conv3D	(11, 7, 7)	(1, 1, 1)	-	(5, 12, 256, 256)
LeakyReLU	-	-	slope: -0.01	(5, 12, 256, 256)
BatchNorm3D	-	-	-	(5, 12, 256, 256)
Conv3D	(11, 7, 7)	(1, 1, 1)	-	(1, 12, 256, 256)
ReLU	-	-	-	(1, 12, 256, 256)
InputRescaling	-	-	scale: 0.01	(1, 12, 256, 256)

Table 9: FourierUNet3D detailed architecture (8 GPUs)

Scale	Repeat	Layer type	Kernel size	Stride	Notes	Shape (C, D, H, W)
1	1	InputScaling	-	-	scale: 0.01	(1, 1, 256, 256)
1	1	Multiscale	(256, 256)	(2, 2)	-	(60, 1, 256, 256)
		FourierConv2D				
		+ ReLU				
		+ BatchNorm2D				
2			(128, 128)	(2, 2)		(60, 1, 128, 128)
3			(64, 64)	(2, 2)		(60, 1, 64, 64)
4			(32, 32)	(2, 2)		(60, 1, 32, 32)
4	1	Reshape2D3D	-	-	-	(5, 12, 32, 32)
3	1	Upsample2D	-	-	-	(5, 12, 64, 64)
3	2	Conv3D	(11, 7, 7)	(1, 1, 1)	-	(5, 12, 64, 64)
		+ ReLU				
		+ BatchNorm3D				
2	1	Upsample2D	-	-	-	(5, 12, 128, 128)
2	2	Conv3D	(11, 7, 7)	(1, 1, 1)	-	(5, 12, 128, 128)
		+ ReLU				
		+ BatchNorm3D				
1	1	Upsample2D	-	-	-	(5, 12, 256, 256)
1	2	Conv3D	(11, 7, 7)	(1, 1, 1)	-	(5, 12, 256, 256)
		+ ReLU				
		+ BatchNorm3D				
1	1	Conv3D	(1, 1, 1)	(1, 1, 1)	-	(1, 12, 256, 256)
		+ ReLU				
1	1	InputRescaling	-	-	scale: 0.01	(1, 12, 256, 256)

UNet). In the decoding path, we use 3D convolutions with kernel size (3, 5, 5), producing 12 3D feature maps each. There are two such convolutions per scale. Note that this requires we reshape the 2D feature maps from the Fourier convolutions to 3D. This is followed by a 1x1 convolution producing the 3D reconstruction output. We show a diagram of this architecture in Figure 1C, and details of this architecture in Table 9.

For our UNet2D, each encoding convolution produced 24 feature maps (except the first scale, for which the first convolution produced 12 feature maps and the second convolution produced 24 feature maps). Each decoding convolution produced 24 feature maps, but took an input of 48 feature maps where 24 feature maps were concatenated from the corresponding encoding convolution at that scale. At the end of the UNet2D, a (1, 1) convolution reduced the 24 final feature maps to 1 feature map. This single feature map is interpreted as the final output of the network, i.e. the reconstructed plane. We allow the UNet2D to have many more feature maps per plane in addition to more layers as compared to the Fourier convolutional network, because these are necessary in order for the network

Table 10: UNet2D detailed architecture (1 per plane)

Scale	Repeat	Layer type	Kernel size	Stride	Notes	Shape (C, D, H, W)
1	1	InputScaling	-	-	scale: 0.01	(1, 1, 256, 256)
1	1	Conv2D + ReLU + BatchNorm2D	(7, 7)	(1, 1)	-	(12, 1, 256, 256)
1	1	Conv2D + ReLU + BatchNorm2D	(7, 7)	(1, 1)	-	(24, 1, 256, 256)
2	1	MaxPool2D	(2, 2)	(2, 2)	-	(24, 1, 128, 128)
2	2	Conv2D + ReLU + BatchNorm2D	(7, 7)	(1, 1)	-	(24, 1, 128, 128)
n	1	MaxPool2D	(2, 2)	(2, 2)	-	(24, 1, $\frac{256}{2^{n-1}}$, $\frac{256}{2^{n-1}}$)
n	2	Conv2D + ReLU + BatchNorm2D	(7, 7)	(1, 1)	-	(24, 1, $\frac{256}{2^{n-1}}$, $\frac{256}{2^{n-1}}$)
8	1	MaxPool2D	(2, 2)	(2, 2)	-	(24, 1, 2, 2)
8	2	Conv2D + ReLU + BatchNorm2D	(7, 7)	(1, 1)	-	(24, 1, 2, 2)
7	1	Upsample2D	-	-	-	(24, 1, 4, 4)
7	2	Conv2D + ReLU + BatchNorm2D	(7, 7)	(1, 1)	-	(24, 1, 4, 4)
n	1	Upsample2D	-	-	-	(24, 1, $\frac{256}{2^{n-1}}$, $\frac{256}{2^{n-1}}$)
n	2	Conv2D + ReLU + BatchNorm2D	(7, 7)	(1, 1)	-	(24, 1, $\frac{256}{2^{n-1}}$, $\frac{256}{2^{n-1}}$)
1	1	Upsample2D	-	-	-	(24, 1, 256, 256)
1	2	Conv2D + ReLU + BatchNorm2D	(7, 7)	(1, 1)	-	(24, 1, 256, 256)
1	1	Conv2D + ReLU	(1, 1)	(1, 1)	-	(1, 1, 256, 256)
1	1	InputRescaling	-	-	scale: 0.01	(1, 1, 256, 256)

to be able to integrate information from a larger field of view. We show the details of our UNet2D architecture in Table 10.

The architecture of the vanilla UNet3D is also 4 scales, with a max pooling factor of 2 per scale in the encoding path and an upsampling factor of 2 in the decoding path. Each scale of the encoding path produces 480 2D feature maps. These are concatenated to the incoming feature maps of the decoding convolutions at the corresponding scale, again with a reshape from 2D to 3D. Each scale of the decoding path produces 48 3D feature maps. Again, this is followed by a 1x1 convolution producing the 3D reconstruction output. All convolutions are in 3D with a kernel size of (5, 7, 7), with the z dimension being ignored for the encoding path because the input is 2D. We show the details of our UNet3D architecture in Table 11.

A.5 Details for microscope optimization depends on sample structure

For our experiments in Section 3.3, we use 64 planes at $1\mu\text{m}$ resolution in z and therefore 64 reconstruction networks to train PSFs. When training reconstruction networks only to produce the higher quality reconstructions, we use 128 planes at $1\mu\text{m}$ resolution in z (chosen so that the planes actually span $250\mu\text{m}$ in z). We train in the reconstruction only setting without any sparse planewise gradients, meaning we image and reconstruct all 128 planes. However, when training a PSF we image

Table 11: UNet3D detailed architecture (8 GPUs)

Scale	Repeat	Layer type	Kernel size	Stride	Notes	Shape (C, D, H, W)
1	1	InputScaling	-	-	scale: 0.01	(1, 1, 256, 256)
1	1	Conv2D + ReLU + BatchNorm2D	(7, 7)	(1, 1)	-	(30, 1, 256, 256)
1	1	Conv2D + ReLU + BatchNorm2D	(7, 7)	(1, 1)	-	(60, 1, 256, 256)
2	1	MaxPool2D	(2, 2)	(2, 2)	-	(60, 1, 128, 128)
2	2	Conv2D + ReLU + BatchNorm2D	(7, 7)	(1, 1)	-	(60, 1, 128, 128)
3	1	MaxPool2D	(2, 2)	(2, 2)	-	(60, 1, 64, 64)
3	2	Conv2D + ReLU + BatchNorm2D	(7, 7)	(1, 1)	-	(60, 1, 64, 64)
4	1	MaxPool2D	(2, 2)	(2, 2)	-	(60, 1, 32, 32)
4	2	Conv2D + ReLU + BatchNorm2D	(7, 7)	(1, 1)	-	(60, 1, 32, 32)
4	1	Reshape2D3D	-	-	-	(5, 12, 32, 32)
3	1	Upsample2D	-	-	-	(5, 12, 64, 64)
3	2	Conv3D + ReLU + BatchNorm3D	(11, 7, 7)	(1, 1, 1)	-	(5, 12, 64, 64)
2	1	Upsample2D	-	-	-	(5, 12, 128, 128)
2	2	Conv3D + ReLU + BatchNorm3D	(11, 7, 7)	(1, 1, 1)	-	(5, 12, 128, 128)
1	1	Upsample2D	-	-	-	(5, 12, 256, 256)
1	2	Conv3D + ReLU + BatchNorm3D	(11, 7, 7)	(1, 1, 1)	-	(5, 12, 256, 256)
1	1	Conv3D + ReLU	(1, 1, 1)	(1, 1, 1)	-	(1, 12, 256, 256)
1	1	InputRescaling	-	-	scale: 0.01	(1, 12, 256, 256)

Table 12: FourierNet2D detailed architecture (1 per plane)

Layer type	Kernel size	Stride	Notes	Shape (C, D, H, W)
InputScaling	-	-	scale: 0.01	(1, 1, 512, 512)
FourierConv2D	(512, 512)	(2, 2)	-	(5, 1, 512, 512)
LeakyReLU	-	-	slope: -0.01	(5, 1, 512, 512)
BatchNorm2D	-	-	-	(5, 1, 512, 512)
Conv2D	(11, 11)	(1, 1)	-	(1, 1, 512, 512)
ReLU	-	-	-	(1, 1, 512, 512)
InputRescaling	-	-	scale: 0.01	(1, 1, 512, 512)

and reconstruct 40 planes at a time with gradient per iteration (spread across 8 GPUs). These 40 planes are chosen randomly at every iteration from the 64 total possible planes, making potentially separate draws of planes for imaging and reconstruction. We show details of all datasets used for training reconstructions in Table 4.

We show the details of our FourierNet2D architecture for training PSFs at the larger field of view in Type A, B, C in Table 12 and our FourierNet3D architecture for training reconstruction networks at

Table 13: FourierNet3D detailed architecture (8 GPUs)

Layer type	Kernel size	Stride	Notes	Shape (C, D, H, W)
InputScaling	-	-	scale: 0.01	(1, 1, 512, 512)
FourierConv2D	(512, 512)	(2, 2)	-	(80, 1, 512, 512)
LeakyReLU	-	-	slope: -0.01	(80, 1, 512, 512)
BatchNorm2D	-	-	-	(80, 1, 512, 512)
Reshape2D3D	-	-	-	(5, 16, 512, 512)
Conv3D	(11, 7, 7)	(1, 1, 1)	-	(5, 16, 512, 512)
LeakyReLU	-	-	slope: -0.01	(5, 16, 512, 512)
BatchNorm3D	-	-	-	(5, 16, 512, 512)
Conv3D	(11, 7, 7)	(1, 1, 1)	-	(1, 16, 512, 512)
ReLU	-	-	-	(1, 16, 512, 512)
InputRescaling	-	-	scale: 0.01	(1, 16, 512, 512)

the larger field of view in Type A, B, C in Table 13. There are no other networks used for these larger field of view experiments. We also show details for training times for both training PSFs and for training more powerful reconstruction networks in Table 6. All PSFs in these networks were trained for the same number of iterations. However, reconstruction networks for some of these experiments were only trained for as long as necessary to converge (with some exceptions where we attempted longer training to check for performance gains with long training periods). Generally, we observed that performance for such reconstruction networks does not meaningfully change with many more iterations of training³.

A.6 Details for Fourier convolutions outperform state-of-the-art learned methods on reconstructing natural images captured by the DiffuserCam lensless camera

Table 14: FourierNetRGB detailed architecture

Layer type	Kernel size	Stride	Notes	Shape (N, C, H, W)
FourierConv2D	(256, 256)	(2, 2)	-	(4, 3, 280, 470)
LeakyReLU	-	-	slope: -0.01	(4, 20, 280, 470)
BatchNorm2D	-	-	-	(4, 20, 280, 470)
Conv2D	(11, 11)	(1, 1)	-	(4, 64, 280, 470)
BatchNorm2D	-	-	-	(4, 64, 280, 470)
LeakyReLU	-	-	slope: -0.01	(4, 64, 280, 470)
Conv2D	(11, 11)	(1, 1)	-	(4, 64, 280, 470)
BatchNorm2D	-	-	-	(4, 64, 280, 470)
LeakyReLU	-	-	slope: -0.01	(4, 64, 280, 470)
Conv2D	(11, 11)	(1, 1)	-	(4, 3, 280, 470)
ReLU	-	-	-	(4, 3, 280, 470)

We performed no augmentations for this set of trainings reconstructing RGB color images of natural scenes from RGB diffused images taken through a DiffuserCam [12]. We modified our FourierNet2D architecture to create the FourierNetRGB architecture, outlined in Table 14. Because these reconstructions are of 2D images only and required no microscope simulation, we were able to use a batch size of 4 images per iteration.

³Training times are approximate, and actual total time was longer due to checkpointing/snapshotting/validation of data and/or differences in load on the clusters being used.

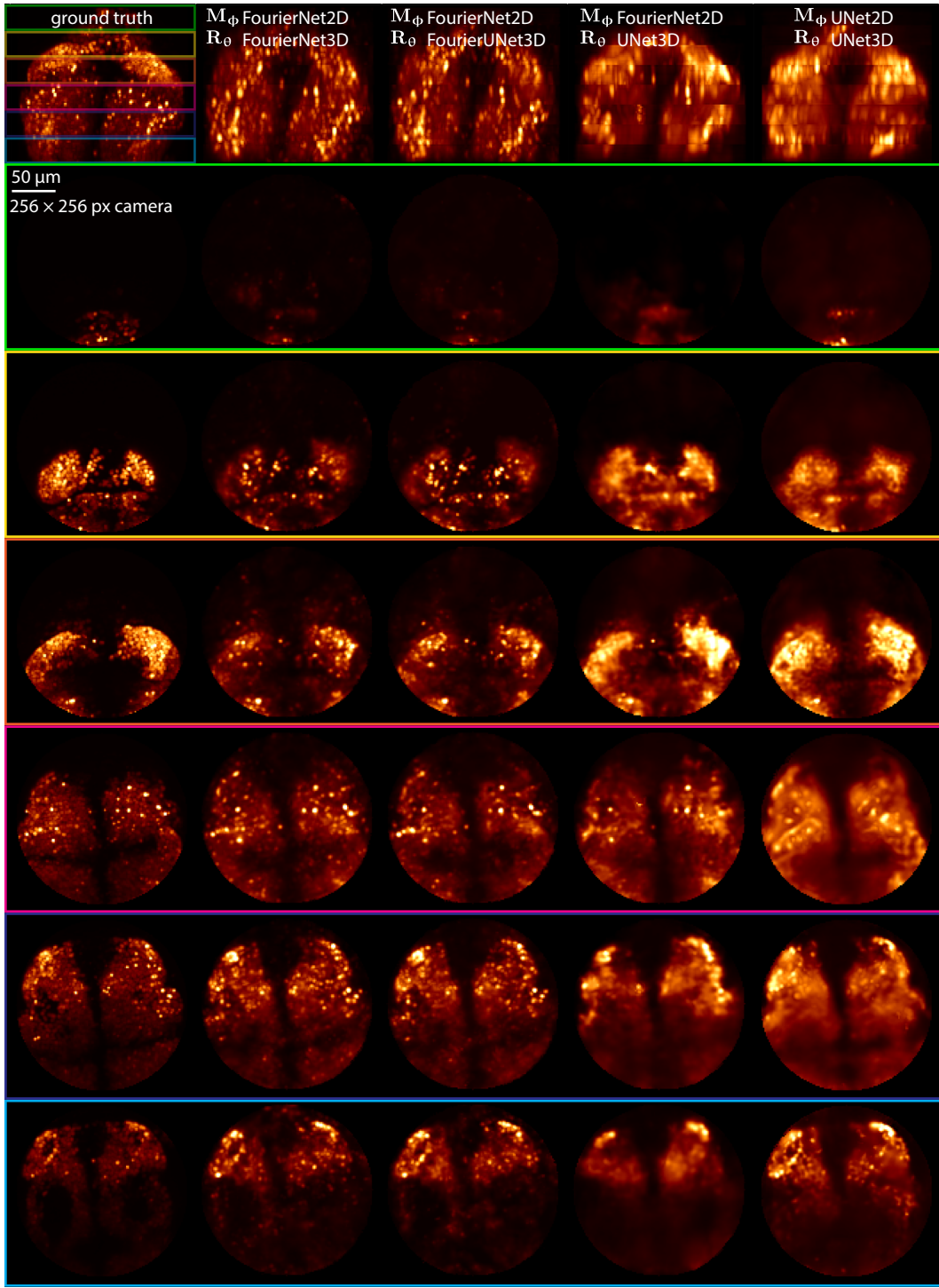


Figure 8: Slab views of a Type D example volume reconstruction, showing our methods (FourierNet/FourierUNet) do the best job of reconstructing throughout the volume. Note that the UNet reconstructions are blurry across all slabs, with few exceptions. Colored boxes show which sample planes a particular slab comes from, corresponding to boxes in xz projection view at top. Annotation M_ϕ shows which network architecture was used for microscope optimization; annotation R_θ shows which architecture was used for reconstruction.

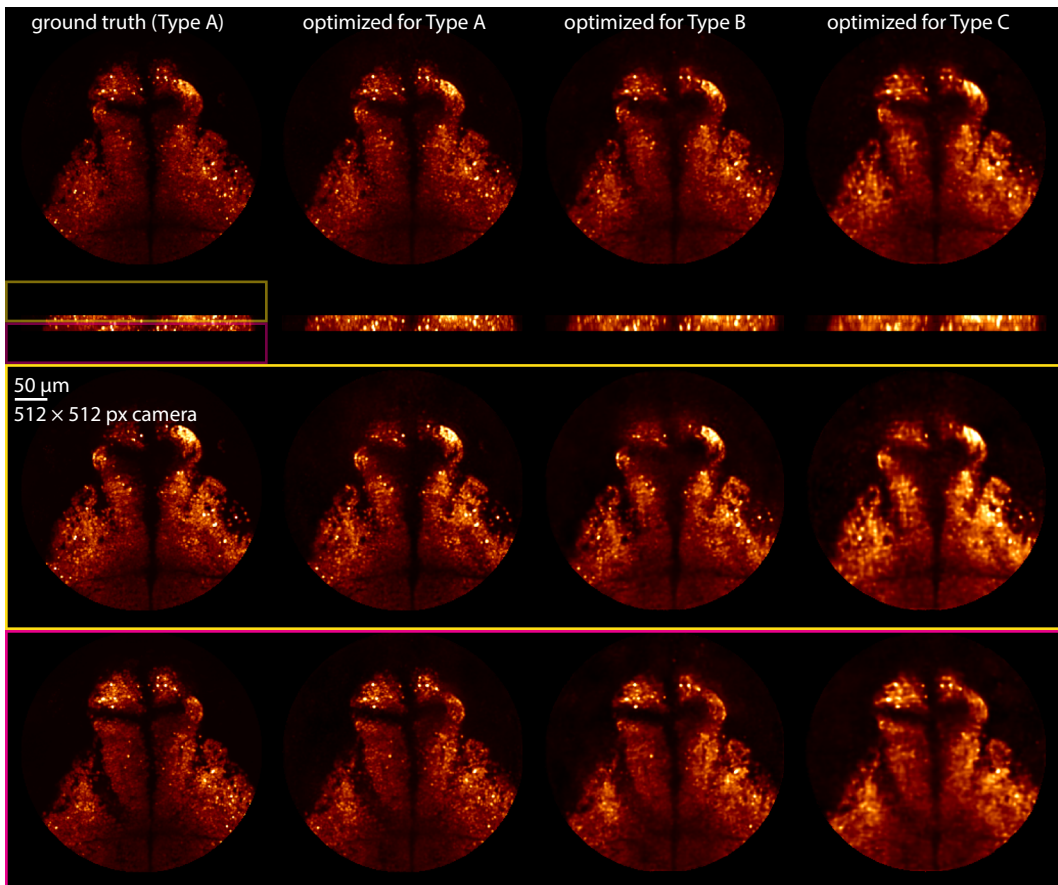


Figure 9: Slab views of an example Type A volume show that the microscope optimized for Type A results in the best reconstructions. Note that the reconstruction with a microscope optimized for Type A is almost identical to the ground truth, while the other microscopes create blurrier reconstructions. Slabs are xy max projections in thinner chunks as opposed to projecting through the entire volume. Colored boxes show which sample planes a particular slab comes from, corresponding to boxes in xz projection view at top.

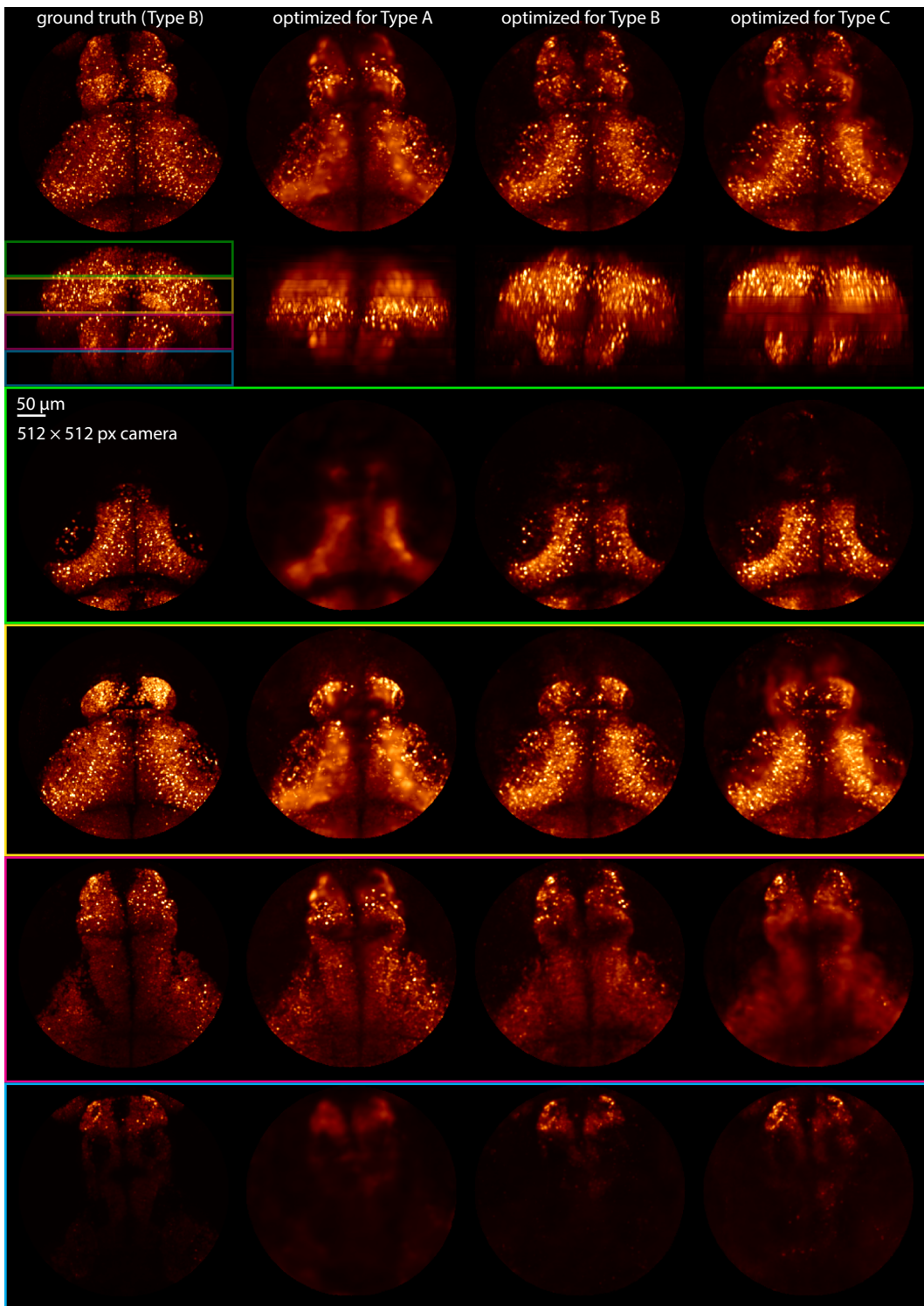


Figure 10: Slab views of an example Type B volume show that the microscope optimized for Type B results in the best reconstructions; other microscopes result in blurrier reconstructions. Colored boxes show which sample planes a particular slab comes from, corresponding to boxes in xz projection view at top.

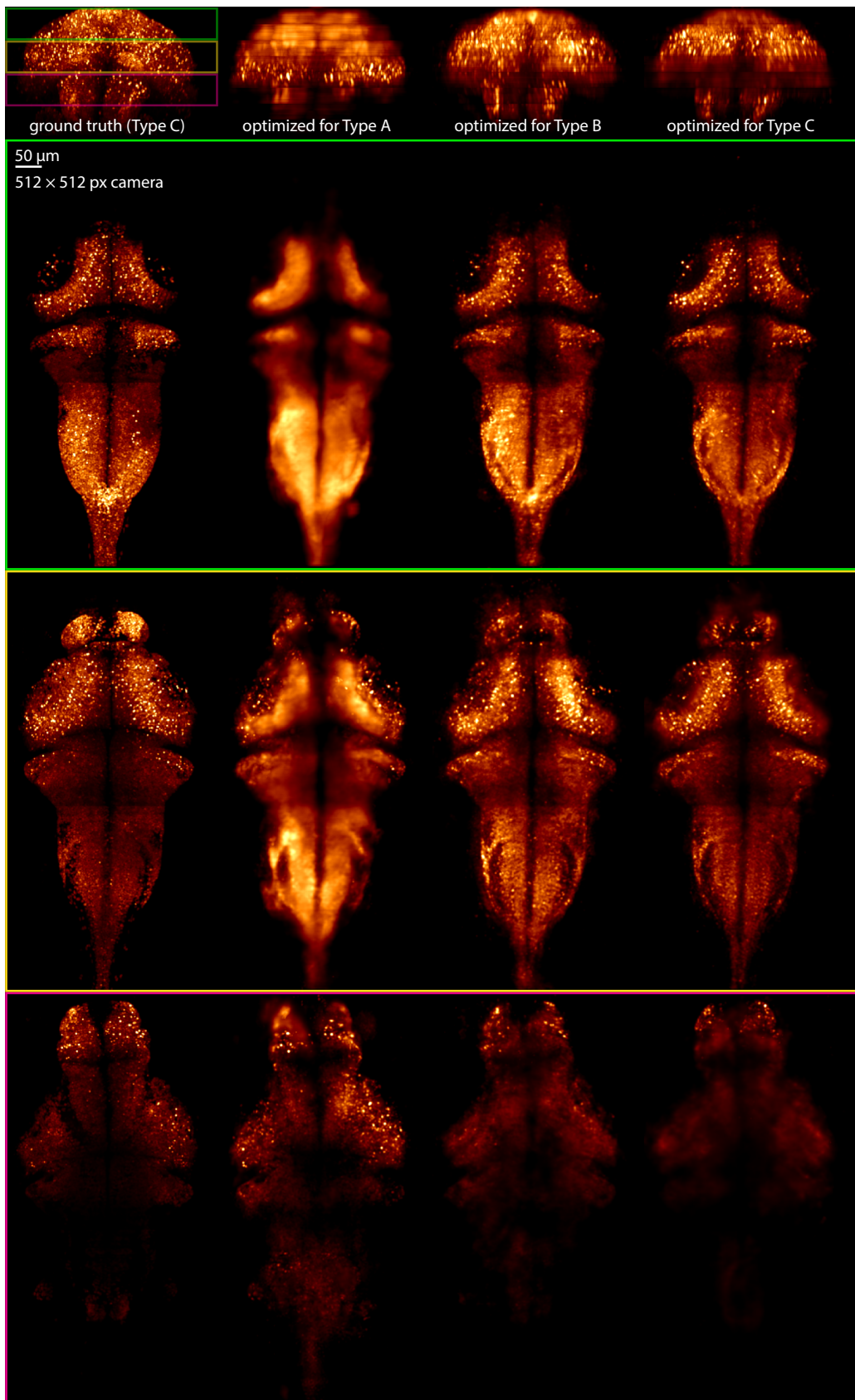


Figure 11: Slab views of an example Type C volume show that microscope optimized for Type C provides most consistent reconstruction. Colored boxes have same meaning as Figures 9, 10.